Applied Energy 401 (2025) 126640

Contents lists available at ScienceDirect

Applied Energy

journal homepage: www.elsevier.com/locate/apenergy

Thermodynamic analysis and performance enhancement of an integrated solar–geothermal polygeneration system using grey wolf optimization and LSTM-based forecasting with Monte Carlo uncertainty analysis: A case study on Tenerife Island

Ali Shokri Kalan [a,*], Mohammadreza Babaei Khuyinrud [b], Farshad Jahangiri [c], Ramin Ahmadi [d], Amir Mahboubi [e], Xiaoshu Lü [a], Marc A. Rosen [f]

[a] *Renewable Energy and Built Environment, University of Vaasa, P.O. Box 700, FIN-65101 Vaasa, Finland*
[b] *Faculty of Mechanical Engineering, Sahand University of Technology, Tabriz, Iran*
[c] *Department of Civil Engineering, Sharif University of Technology, Tehran, Iran*
[d] *Department of Building, Civil and Environmental Engineering, Concordia University, Montréal, Canada*
[e] *Department of Mechanical Engineering, Tabriz University, Tabriz, Iran*
[f] *Faculty of Engineering and Applied Science, University of Ontario Institute of Technology, Oshawa, Ontario L1G 0C5, Canada*

HIGHLIGHTS

- A case study on an efficient polygeneration system using solar and geothermal energy.
- Green multi-generation for power, heating, cooling, hydrogen, and freshwater.
- Energy and exergy analyses, showing high efficiency and performance.
- LSTM forecasting of solar irradiance for reliable system planning.
- Grey wolf optimization and uncertainty analysis using Monte Carlo.

GRAPHICAL ABSTRACT

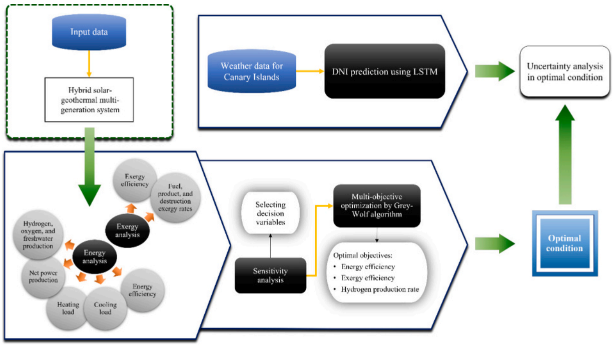

ARTICLE INFO

Keywords:
Sustainable hybrid renewable
Solar and geothermal
Green hydrogen production
seq2seq LSTM forecasting
Monte Carlo analysis
Grey wolf optimization

ABSTRACT

Global warming and fossil fuel supply limitations highlight the need for sustainable energy options. Renewable-based systems provide a path to carbon neutrality but face reliability challenges due to intermittency. This study investigates Tenerife Island's potential for integrating solar and geothermal energy. A novel hybrid system is proposed, combining concentrated solar power, geothermal energy resources, with a system comprised of the following components: a supercritical CO₂ cycle, a lithium bromide-water absorption cooling system, a multi-effect desalination unit, a three-stage organic Rankine cycle and a proton exchange membrane electrolyzer. This system produces electricity, heating, cooling, freshwater, and hydrogen, achieving baseline energy and exergy efficiencies of 62 % and 17, respectively. The system's production rates are 7844 kW power, 4416 kW cooling, 6848 kW heating, 22.6 kg/h hydrogen, and 20.7 m^3/h freshwater. Optimization using the grey wolf

---

* Corresponding author.
E-mail address: Ali.Shokrikalan@uwasa.fi (A.S. Kalan).

https://doi.org/10.1016/j.apenergy.2025.126640
Received 27 April 2025; Received in revised form 12 July 2025; Accepted 10 August 2025

algorithm enhances the energy efficiency by 21 %, the exergy efficiency by 38 %, and the hydrogen production rate by 18 %. Solar energy forecasting employs direct normal irradiance data (2005–2024) with seq2seq long short-term memory predictions up to 2030. A forward uncertainty analysis using Monte Carlo simulations reveals that cooling capacity, exergy destruction rate, and net power production are most sensitive to fluctuations in direct normal irradiance, with coefficients of variation (CV) ranging from 4.4 % to 4.5 %, while energy and exergy efficiencies exhibit minimal coefficient of variation (CV < 0.1 %).

Nomenclature

A	Area (m^2)
ABS	Absorber
BFR	Brine flow ratio
BHI	Beam horizontal irradiance (W/m^2)
COND	Condenser
CSP	Concentrated solar power
D	Thickness of membrane (m)
DHI	Diffuse Horizontal Irradiance (W/m^2)
DNI	Direct normal irradiance (W/m^2)
DWH	District water heating
$\dot{E}$	Exergy rate (kW)
EVA	Evaporator
F	Faraday constant
G	Gibbs free energy (kJ/kmol)
GEN	Generator
GHI	Global horizontal irradiance (W/m^2)
h	Specific enthalpy (kJ/kg)
H_2	Hydrogen
HEX	Heat exchanger
HTR	High temperature recuperator
J	Current density (A/m^2)
LSTM	Long short-term memory
LTR	Low temperature recuperator
$\dot{m}$	Mass flow rate (kg/s)
MC	Main compressor
MED-MVC	Multi-Effect Desalination, Mechanical Vapor Compression
N	Number of heliostats
$\dot{n}$	Molar flow rate (kmol/s)
O_2	Oxygen
ORC	Organic Rankine cycle
P	Pressure (bar)
PEM	Proton exchange membrane
PD	Pressure drop (%)
PR	Pressure ratio
$\dot{Q}$	Heat transfer rate (kW)
R	Ohmic resistance (Ω)
RC	*Re*-compressor
RMSE	Root mean wquare error (%)
s	Specific entropy (kJ/kgK)
S	Salinity
s-CO_2	Supercritical CO_2
SHE	Solution heat exchanger
SR	Split ratio
T	Temperature (K)
TEG	Thermoelectric generator
TTD	Terminal temperature difference (K)
TUR	Turbine
V	Cell potential, voltage (volt)
$\dot{W}$	Electrical power (kW)
X	LiBr mass fraction (%)
y_d	Exergy destruction ratio (%)
ZT_m	Efficiency of thermoelectric material

Greek symbols

$\boldsymbol{\Delta}$	Difference
η_I	Energy efficiency (%)
η_{II}	Exergy efficiency (%)
ε	Effectiveness (%)
λ	Hydration factor
$\sigma(x)$	Local ionic conductivity of PEME membrane (S/m)

Subscripts

0	Dead state, at ambient T and P
an	Anode
att	Atmospheric attenuation
ca	Cathode
ch	Chemical
cos	Cosine effect
D	Destruction
e	Outlet
F	Fuel exergy
H	High
hel	Heliostat
i	Inlet
int	Interception
is	Isentropic
k	k^{th} component
L	Low
min	Minimum
P	Product exergy
ph	Physical
PP	Pinch point
rec	Receiver
ref	Reference
refl	Reflectivity of heliostat
s&b	Shading and blocking
sol	Solution
ss	Strong solution
th	Thermomechanical
ws	Weak solution

1. Introduction

The link between population growth, urbanization, and rising energy demand has major environmental consequences, especially in terms of increased CO_2 emissions and changes to global climate patterns. [1]. Moreover, fossil fuel reservoirs are limited, and they will become increasingly depleted over time [2]. The growing demand for energy, coupled with the need to reduce emissions, has driven humanity to accelerate the transition to renewable energy sources and improve the efficiency of energy systems [3]. To improve system efficiency, one strategy can involve implementing polygeneration (often referred to as multigeneration) energy systems, including combined heat and power (CHP), combined cooling, heating, and power (CCHP) systems [4], as well as systems that produce additional outputs such as freshwater [5] while ensuring the effective use of subsystems. Additionally, the strategic implementation of waste heat recovery (WHR) technology, including the incorporation of novel thermoelectric generator (TEG) technology during the establishment of the energy systems, is potentially beneficial. Various efficient cycles can serve as subsystems, including organic Rankine cycles [6], supercritical CO_2 cycles [7], Kalina cycles [8], gas turbine cycles [9], and desalination systems for freshwater production. There are several renewable energy sources that can drive energy systems, including solar, wind, geothermal [10], biomass, and hydropower [11]. Solar-based energy systems, which include concentrated solar power (CSP) systems [12] and photovoltaic solar panels [13], along with wind turbines, hydropower, and geothermal systems, can be collectively referred to as clean energy systems. These systems have the potential to achieve net-zero emissions [14].

Many studies rely on a single renewable energy source. Jin et al. [15] conducted a solar-powered CHP system that incorporates an organic Rankine cycle and a heat pump. Using a composite sustainability index, they found that a 75 % heat distribution scenario achieved the best performance. Sensitivity analysis showed strong links between solar input and emission reductions, and between electricity prices and cost savings. Ghorbani [16] developed a geothermal CCHP system with Kalina cycle, organic Rankine cycle and ejector refrigeration. Using TOPSIS optimization, the study found a thermal efficiency of about 23 % and a cost of $45,900 per year at 490 K. Higher heat source temperatures and ammonia concentrations reduce efficiency and raise costs.

Relying on a single renewable energy source can be effective but poses sustainability challenges. A more sustainable, zero-emission energy system can be achieved through hybrid renewable sources. Fu et al. [3] investigated a hybrid solar-wind system integrated with liquid CO_2 energy storage (LCES) to enhance efficiency and stability. The combined system achieved a 94.6 % overall efficiency, surpassing standalone wind-LCES (80.3 %) and solar-LCES (76.3 %) setups. However, practical implementation requires studying the potential for using multiple renewable sources in specific regions, which has been explored in only a few studies. Qian et al. [17] conducted a study in China to evaluate a wind-solar-CCHP system using emergy theory and multi-objective decision-making. A case study at a hotel in western China showed the wind-solar-CCHP system outperformed traditional CCHP, offering a more effective approach for optimizing new energy use.

In arid and semi-arid regions, water scarcity represents a significant challenge. To address this, some polygeneration energy systems are designed to produce freshwater as a byproduct. Various desalination technologies have been integrated into these systems, with reverse osmosis (RO) [18], humidification-dehumidification (HDH), and multi-effect distillation (MED) being among the most commonly utilized methods. Forghani et al. [19] proposed a solar-geothermal hybrid multigeneration system using MED for freshwater production at a hotel in Bandar Abbas, Iran. The integration of renewables reduced annual costs by up to 59.8 %, with the combined setup offering the greatest economic savings.

In addition to integrating hybrid renewable energy sources to achieve sustainability, several strategies can enhance the reliability and efficiency of sustainable energy systems. Waste heat recovery, using advanced technologies like thermoelectric generation (TEG), enables direct conversion of waste heat to electricity [20]. Another key method is thermal energy storage (TES), which stores energy in thermal form for later use, particularly valuable when the primary energy source is intermittent or unavailable. Ran et al. [21] developed a biogas-driven system with SOFC, waste heat recovery, and solar thermal storage. The storage integration improved performance, delivering 351.4 kW net power with energy and exergy efficiencies of 43.3 % and 37.4 %. Mehrpooya et al. [22] investigated a solar-assisted Kalina cycle integrated with flat plate collectors and phase change material (PCM) for thermal energy storage. Located in Bandar Abbas, the system achieved an annual solar fraction of 83.8 %, with PCM supplying heat during non-solar hours. The PCM storage plays a key role in maintaining continuous operation, reducing the auxiliary heater's share to only 8.72 GWh annually.

Producing and storing green hydrogen can enhance the sustainability of renewable energy systems. The hydrogen can power fuel cells, be converted to fuels, or be used directly without harmful emissions. Green hydrogen is generated from water via electrolyzers using surplus renewable energy. Electrolyzers used for hydrogen generation fall into three main types: proton exchange membrane [23], solid oxide [24], and alkaline electrolyzers [25]. Superchi et al. [26] examined the coupling wind power with alkaline electrolyzers for green hydrogen production. They simulated three module capacities (1, 2, and 4 MW) alongside a 13.8 MW wind farm, aiming to minimize the levelized cost of hydrogen. Arias et al. [27] optimized proton exchange membrane electrolyzers with photovoltaic systems for hydrogen production, showing that grid integration and excess solar energy can lower the levelized cost of hydrogen, even in low-solar resource areas.

Enhancing energy systems and establishing optimal operational parameters are important for improving their efficiencies. Several optimization techniques have been investigated to improve CCHP systems, including the improved multi-objective multi-verse optimizer (IMOMVO), ant colony optimization (ACO), genetic algorithms, and multi-objective particle swarm optimization (MOPSO) [28]. Jesús Águila-León et al. [29] combined the grey wolf optimizer (GWO) with particle swarm optimization (PSO) to enhance a maximum power point tracking (MPPT) controller in solar energy systems. Tested in MATLAB/Simulink, the GWO-PSO improved energy generation by 20.7 %.

Uncertainty in model-based energy systems involves several aspects, including aleatory (random), epistemic (knowledge-based), and input uncertainties. These uncertainties arise when variable inputs are treated as constant, and are also influenced by factors such as design choices, operational conditions, system degradation, and maintenance schedules [30]. In addition, economic and regulatory factors, such as energy price volatility and policy changes, further contribute to the complexity of ensuring system reliability [31].

It is important to include both uncertainty analysis and forecasting in renewable-based energy systems. Hoang et al. proposed [32] a hierarchical framework to minimize emissions while addressing forecast uncertainty in renewable energy. A key feature of the study is the use of probabilistic forecasting with data-driven stochastic differential equations to model uncertainties like solar irradiance and wind variability. This approach enables the use of less conservative probabilistic constraints, improving the reliability and flexibility of energy management under uncertainty.

Direct normal irradiance (DNI) is a vital input parameter in solar energy systems, with its uncertainty stemming from multiple sources. Principal contributors to DNI variability include atmospheric factors such as cloud cover, inter-annual variability, aerosol concentrations, and water vapor content, alongside seasonal and geographic fluctuations [33]. DNI uncertainty significantly affects solar energy systems, impacting system efficiency and supply stability. Inaccurate DNI data can lead to suboptimal designs, inefficient energy dispatch, higher operational costs, and challenges in long-term planning and investment due to unreliable performance predictions [34]. Many studies treat DNI as a fixed input, overlooking its uncertainty. Quantifying this uncertainty is important for assessing system resilience and supporting sustainable energy decisions. The current study introduces a probabilistic framework using long short-term memory (LSTM) neural networks and Monte Carlo simulations to evaluate DNI uncertainty—due to variability and measurement errors—on energy outputs. By analyzing data from 2005 to 2030, the framework quantifies input uncertainty and reveals how DNI fluctuations affect system performance and resilience, aiding in the design of reliable energy systems and optimized strategies.

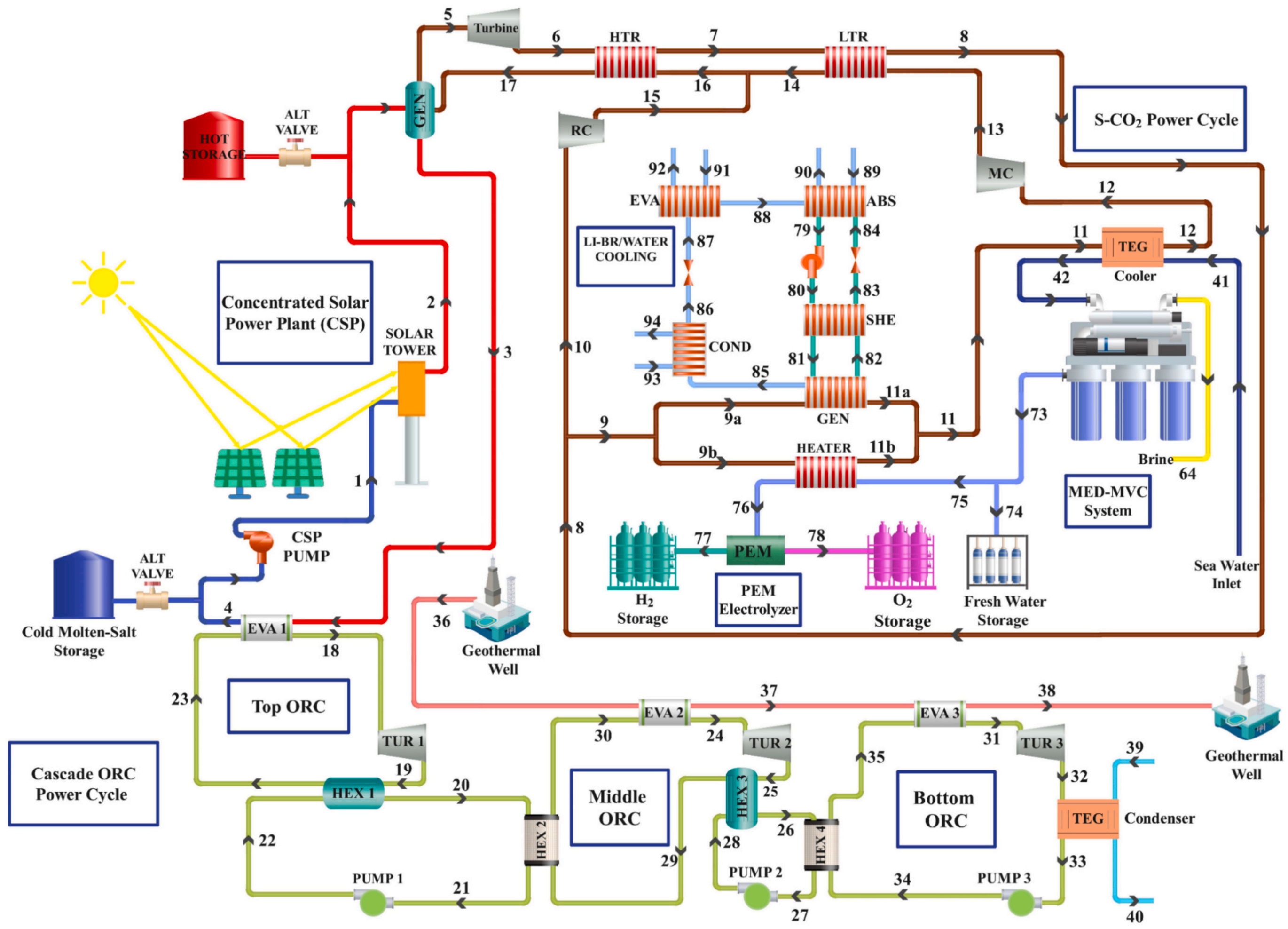

Fig. 1. Schematic of the proposed polygeneration system.

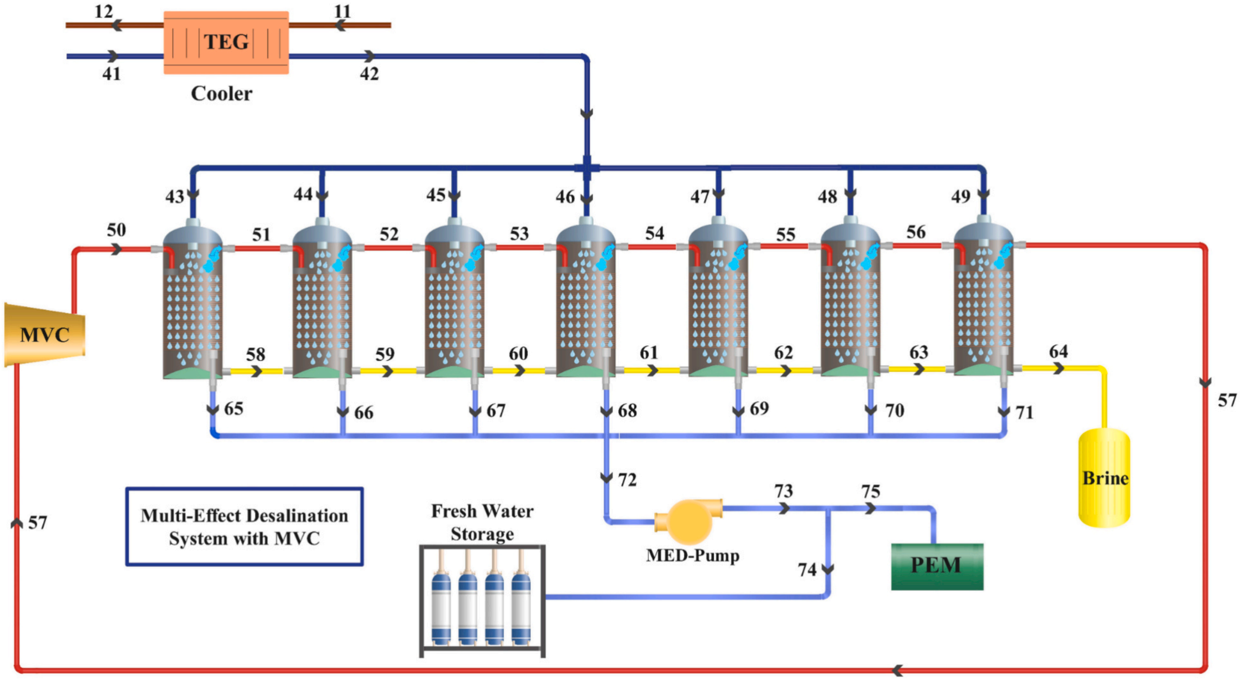

Fig. 2. Schematic of the MED-MVC system.

Although numerous studies have investigated renewable-based energy systems, most have focused on single-source configurations, with fewer exploring integrated or application-specific designs. Some works introduce hybrid renewable systems without grounding them in real-world case areas or assessing the local potential for hybrid deployment. Many studies also overlook the integration of waste heat recovery technologies, which can significantly enhance system efficiency. Proposing truly sustainable renewable-based energy systems is increasingly important, yet there is insufficient research on this, particularly in addressing the uncertainty of energy systems, and when it is explored, it is often on a small scale.

This study aims to develop and evaluate a sustainable, large-scale polygeneration energy system designed for Tenerife Island. The proposed solar–geothermal hybrid configuration integrates CSP, a supercritical CO_2 cycle, a LiBr–water absorption system, a three-stage ORC, and a multi-effect desalination with mechanical vapor compression (MED-MVC) unit to produce electricity, heating, cooling, and freshwater. Various waste heat recovery technologies, such as thermoelectric generators, have been applied to improve system efficiency, and an electrolyzer is included to produce hydrogen and further enhance overall sustainability. The system is assessed through energy and exergy analyses, followed by sensitivity analysis and multi-objective optimization using the grey wolf method. Real satellite data specific to the case area are used, with key variables forecasted up to 2030 using a long short-term memory model. A Monte Carlo-based uncertainty analysis is also performed to evaluate system reliability under varying conditions.

The originality and key contributions of this research are outlined as follows:

- Development of a novel and sustainable solar–geothermal polygeneration system
- Comprehensive thermodynamic analysis and multi-objective optimization
- Integration of forecasting and uncertainty analysis in system design

2. System description

Figs. 1 and 2 illustrate the configuration of the proposed novel polygeneration system, driven by solar–geothermal energy sources. The system integrates a CSP unit, a supercritical CO_2 cycle, a three-stage ORC, a LiBr–water absorption system, a MED–MVC desalination unit, and a PEM electrolyzer. It is designed to simultaneously produce power, heating, cooling, hydrogen, and freshwater.

2.1. Concentrated solar power plant

Fig. 1 illustrates a schematic in which heliostats track the sun and reflect sunlight onto a central receiver atop a solar tower, thereby raising its temperature. The receiver transfers a portion of this absorbed energy to the molten salt, while the remainder is lost to the environment through convective, conductive, and reflective heat losses. Molten salt, pressurized by PUMP 1 (state 1), is heated in the tower (state 2) and serves as the hot stream for the s-CO_2 cycle. After leaving the s-CO_2 generator (state 3), residual energy powers the cascade ORC power cycle via EVA 1, with the salt returning to PUMP 1 (state 4). Hot and cold molten salt storages manage mass flow rates for operational flexibility and energy efficiency.

2.2. Supercritical CO_2 subsystem

The high-temperature, high-pressure stream (state 5) enters the turbine to generate power, and then preheats the cold stream in the high-temperature recuperator (HTR) (state 6) and the low-temperature recuperator (LTR) (state 7). Exiting the LTR (state 8), the stream splits into stream 10 and stream 9. Stream 10, pressurized in the recompression compressor (RC) (state 15), mixes with the LTR stream (state 14), passes through the HTR (state 16), and is heated in the supercritical CO_2 generator (s-CO_2 Gen). Stream 9 splits further: stream 9a powers the Li-Br/water cooling system, and stream 9b supplies heat for hydrogen generation in the PEM electrolyzer. Streams 11a and 11b combine into stream 11, which generates electricity in the thermoelectric generator (TEG) and supports freshwater production in the MED-MVC system. Exhaust from the TEG (state 12) enters the main compressor (MC), then the LTR (state 13), before mixing with state 15 (state 14).

2.3. LiBr/Water absorption cooling system

In the generator (GEN) shown in Fig. 1, the LiBr/water mixture is heated, separating into a concentrated LiBr/water solution (state 82) and refrigerant vapor (H_2O) (state 85). The concentrated solution is heated in the solution heat exchanger (SHE) (state 83), expanded (state 84), and sent to the absorber (ABS) to absorb refrigerant vapor. In the condenser (COND), refrigerant vapor condenses to a high-pressure liquid refrigerant (state 86), is expanded (state 87), and moves to the evaporator (EVA), where it evaporates at low pressure and temperature (state 88), cooling the water (states 91–92). In the absorber, the LiBr/water solution absorbs refrigerant vapor from the evaporator (state 84). The weak solution (state 79) is pressurized by a pump (state 80), is preheated in the SHE (state 81), and returns to the GEN, completing the cycle.

2.4. MED-MVC system

The MED-MVC desalination subsystem, shown in Fig. 2, is designed for efficient freshwater production and includes seven effects, a vapor compressor, and a pump. Seawater (state 41) enters the TEG for heating, and then divides into equal seven streams, each entering one effect. Saturated vapor is compressed and superheated in the mechanical vapor compressor (MVC). For optimized heat transfer, seawater is sprayed into effect chambers as the superheated vapor enters. Each effect produces three streams: saturated vapor, freshwater, and brine. The vapor transfers thermal energy sequentially to each stage, with its energy progressively decreasing until it is boosted back to the initial level by an external power source. Freshwater (blue line) and brine (yellow line) are the remaining outputs.

2.5. Proton exchange membrane electrolyzer

As shown in Fig. 1 and Fig. 2, the freshwater produced (state 72) is pressurized by the MED pump (state 73) and split into two streams: one for domestic use (state 74) and the other for hydrogen production (state 75). Freshwater for hydrogen production is heated in a heater (state 76) to meet the PEM process temperature requirements, resulting in hydrogen (state 78) and oxygen (state 77), which are stored. The freshwater distribution between domestic use and hydrogen production is adjustable based on demand.

2.6. Cascade ORC power cycle

This subsystem includes three stages—top, middle, and bottom ORC—using toluene as the working fluid. Toluene is selected because of its low global warming potential. The working fluid absorbs heat in EVA 1 at state 23, then enters TUR 1 to generate power (state 18). The turbine outlet (state 19) preheats the cold stream entering HEX 1 at state 22. The heated fluid (state 20) serves as the hot stream to preheat the middle ORC before being pressurized by PUMP 2 (state 21) and returning to HEX 1 (state 22).

The preheated flow (state 30) then enters EVA 2, where it absorbs heat from geothermal hot water (states 36–37), reaching a high temperature. The outlet (state 24) expands in TUR 2, releasing heat in HEX 3 (state 25), with additional preheating in HEX 2 (state 29). A separate loop absorbs heat from HEX 3 for the bottom ORC.

Table 1
Operating and design parameters used for the thermodynamic modeling and analysis of the system.

Parameter	Value	Unit	Reference
Concentrated solar power			
DNI	694.5838	(W/m^2)	
η_{cos}	0.8267	–	[38]
$\eta_{s\&b}$	0.9698	–	[38]
η_{int}	0.9710	–	[38]
η_{att}	0.9383	–	[38]
η_{refl}	0.88		[38]
N_{hel}	624	–	[38]
$A_{hel}(width \times length)$	9.45 × 12.84	(m^2)	[38]
A_{rec}	68.1	(m^2)	[38]
Supercritical CO_2 cycle			
PR	3.09	–	[39]
T_{max}	823.15	K	[39]
$\eta_{is,comp}$	85	%	[39]
$\eta_{is,turb}$	90	%	[39]
ε_{HEX}	86	%	[39]
dP_{LTR}	2	%	[39]
dP_{HTR}	3	%	[39]
dP_{DWH}	1	%	[39]
$\Delta T_{pp,GEN}$	3	K	[39]
P_6	74	bar	[39]
$\Delta T_{pp,DWH}$	5	K	[39]
X_{s-CO2}	0.25	–	[39]
LiBr/water cooling system			
T_{89}	298.1	K	[40]
T_{90}	303.15	K	[40]
T_{91}	288.15	K	[40]
T_{92}	283.15	K	[40]
T_{93}	298.15	K	[40]
T_{94}	303.15	K	[40]
T_{85}	348.15	K	[41]
T_{79}	278.15	K	[40]
T_{86}	278.15	K	[40]
T_{88}	308.15	K	[40]
η_{pump}	90	%	[40]
ε_{SHE}	75	%	[40]
MED-MVC			
S_0	35	(g/kg)	[42]
$\overline{e}^0{}_{ch,water}$	45	(kJ/kmol)	[43]
TTD_h	10	K	[44]
$\eta_{is,comp}$	90	%	[44]
Temperature difference between each effect, ΔT_{effect}	1.35	K	[35]
Distilled water temperature of first effect, T_{65}	334.15	K	[45]
η_{pump}	0.9	–	[44]
BFR	0.9	–	[35]
PEME			
Cell temperature	353	K	[46]
Cell pressure	1	bar	[46]
Current density (J)	6000	A/m^2	[46]
Active surface area	0.01	m^2	[46]
Membrane thickness (D)	50	μm	[46]
$\eta_{is,pump}$	85	%	[46]
λ_{an}	14	–	[46]
λ_{ca}	10	–	[46]
Three-stage ORC			
$\eta_{is,tur}$	85	%	[47]
$\eta_{is,p1,2,3}$	80	%	[47]
ΔT_{eva}	10	K	[47]
$\varepsilon_{HEX2,4}$	70	%	[47]
$\Delta T_{HEX1,2}$	10	K	[47]
Geothermal source			
T_{36}	513.15	K	[48]
$\dot{m}_{36}$	1	(kg/s)	[48]
T_{38}	313.15	K	[48]
TEG			
ZT_m	0.8	–	[49]

After preheating in HEX 4, the working fluid (state 35) gains heat from hot streams (states 37–38) and enters TUR 3 for power generation (state 31). The turbine outlet (state 32) transfers heat to cold water (states 39–40), generating electricity in the TEG, before entering PUMP 4 (state 33) and re-joining the preheating process in HEX 4.

3. Methodology

To ensure a precise thermodynamic evaluation of the proposed system, energy, exergy, and sensitivity analyses are conducted using EES software, chosen for its comprehensive and reliable library. Additionally, uncertainty analysis, forecasting, and optimization were performed in the MATLAB environment.

3.1. Mathematical model of the proposed system

This section outlines the thermodynamic models of the subsystems, including the following: CSP, supercritical CO_2 cycle, three-stage ORC, PEM electrolyzer, LiBr/water cooling, and MED-MVC unit. The following assumptions are made:

- All system components operate under steady-state conditions.
- Pressure losses and heat wastes in the pipelines are assumed to be zero.
- The kinetic and potential energy contributions are negligible.
- There are no leaks of the working fluid in the system.
- Pumps, compressors, turbines and MVC are modelled using isentropic efficiencies.
- The temperatures of the outlet brine and steam in each effect are equal [35].
- Seawater enters at dead state conditions [36].
- The refrigerant at the outlets of the COND and ABS is in a saturated liquid and saturated vapor state, respectively [37].
- The temperature of the generator is set to be 5 K lower than the operating temperature of the PEM electrolyzer [37].

The ambient temperature and pressure are assumed to be 293.15 K and 1 bar, respectively. The system has been simulated under the average July DNI conditions for the year 2024. Table 1 presents the operating and design parameters used in the thermodynamic modeling and analysis of the system.

The primary tools employed for the mathematical modeling of the proposed system are based on the fundamental principles of energy and mass conservation. In general, applying energy and mass balances to a given component yields the following equations:

$$\dot{Q}-\dot{W}+\sum_i \dot{m}_i\left(h_i+\frac{V_i^2}{2}+gz_i\right)-\sum_e \dot{m}_e\left(h_e+\frac{V_e^2}{2}+gz_e\right)=\frac{dE}{dt} \tag{1}$$

$$\sum_i \dot{m}_i=\sum_e \dot{m}_e \tag{2}$$

Additionally, by ignoring variations in potential and kinetic exergy, the physical exergy can be calculated as follows [50]:

$$\dot{E}_{ph}=\dot{m}(h-h_0)-T_0(s-s_0) \tag{3}$$

Also, the chemical exergy rate of a substance can be written as [51]:

$$\dot{E}_{ch}=\frac{\dot{m}_k}{M_k}\overline{e}_k^{ch} \tag{4}$$

where M_k is the molecular weight of species k, and $\overline{e}_k^{ch}$ is the chemical exergy per mole of species k. The chemical exergy of LiBr-water solution in the Absorption Cooling System can be expressed as follows [52]:

$$\dot{E}_{ch}=\frac{\dot{m}}{M_{sol}}\left[\sum_k x_k\overline{e}_k^{ch}+\overline{R}T_0\sum_k x_k\ln(a_k)\right] \tag{5}$$

Table 2
Energy and exergy rate balance equations of components in the CSP subsystem.

Component	Energy rate balance	Exergy rate balance
Heliostat field	$\dot{Q}_{rec,in} = \eta_{field}\cdot(DNI).A_{hel}.N_{hel}$	$\dot{E}_D = \dot{Q}_{sun}\left(1-\frac{T_0}{T_{sun}}\right) - \dot{Q}_{rec,in}\left(1-\frac{T_0}{T_{hel}}\right)$
Receiver	$\eta_{rec} = \frac{\dot{Q}_{rec,net}}{\dot{Q}_{rec,in}}$ $\dot{Q}_{rec,in} = \dot{Q}_{rec,net} + \dot{Q}_{rec,loss}$ $\dot{Q}_{rec,net} = \dot{m}_2(h_2 - h_1) + \dot{Q}_{rec,loss}$	$\dot{E}_1 + \dot{Q}_{rec.in}\left(1-\frac{T_0}{T_{ref,hel}}\right) = \dot{E}_2 + \dot{Q}_{rec,loss} + \dot{E}_{D,rec}$
CSP pump	$\dot{W}_{pump,CSP} = \dot{m}_1(h_1 - h_4)$	$\dot{E}_p = \dot{W}_{pump,CSP} - \left(\dot{E}_1 - \dot{E}_4\right)$

Table 3
Energy and exergy rate balance equations of components in s-CO_2 subsystem.

Components	Energy rate balance	Exergy rate balance
GEN	$\dot{m}_2(h_2 - h_3) = \dot{m}_5(h_5 - h_{17})$	$\dot{E}_D = \left(\dot{E}_2 - \dot{E}_3\right) - \left(\dot{E}_5 - \dot{E}_{17}\right)$
HTR	$\dot{m}_6(h_6 - h_7) = \dot{m}_{16}(h_{17} - h_{16})$ $\varepsilon_{HTR} = \frac{T_6 - T_7}{T_6 - T_{16}}$	$\dot{E}_D = \left(\dot{E}_6 - \dot{E}_7\right) - \left(\dot{E}_{17} - \dot{E}_{16}\right)$
LTR	$\dot{m}_7(h_7 - h_8) = \dot{m}_{13}(h_{14} - h_{13})$ $\varepsilon_{LTR} = \frac{T_7 - T_8}{T_7 - T_{13}}$	$\dot{E}_D = \left(\dot{E}_7 - \dot{E}_8\right) - \left(\dot{E}_{14} - \dot{E}_{13}\right)$
TUR	$\dot{W}_{TUR} = \dot{m}_5(h_5 - h_6)$	$\dot{E}_D = \left(\dot{E}_5 - \dot{E}_6\right) - \dot{W}_{TUR}$
MC	$\dot{W}_{MC} = (1 - X_{s-CO2})\,\dot{m}_8(h_{13} - h_{12})$	$\dot{E}_D = \dot{W}_{MC} - \left(\dot{E}_{13} - \dot{E}_{12}\right)$
RC	$\dot{W}_{RC} = X_{s-CO2}.\dot{m}_8(h_{15} - h_{10})$	$\dot{E}_D = \dot{W}_{RC} - \left(\dot{E}_{15} - \dot{E}_{10}\right)$
Cooler	$\dot{m}_{11}(h_{11} - h_{12}) = \dot{m}_{41}(h_{42} - h_{41})$	$\dot{E}_D = \left(\dot{E}_{11} - \dot{E}_{12}\right) - \left(\dot{E}_{42} - \dot{E}_{41}\right)$
Heater	$\dot{m}_{9b}(h_{9b} - h_{11b}) = \dot{m}_{75}(h_{76} - h_{75})$	$\dot{E}_D = \left(\dot{E}_{9b} - \dot{E}_{11b}\right) - \left(\dot{E}_{76} - \dot{E}_{75}\right)$
Mix1	$\dot{m}_{15}h_{15} + \dot{m}_{14}h_{14} = \dot{m}_{16}h_{16}$	$\dot{E}_D = \left(\dot{E}_{14} + \dot{E}_{15}\right) - \dot{E}_{16}$
Mix2	$\dot{m}_{11a}h_{11a} + \dot{m}_{11b}h_{11b} = \dot{m}_{11}h_{11}$	$\dot{E}_D = \left(\dot{E}_{11a} + \dot{E}_{11b}\right) - \dot{E}_{11}$
Spl1	$\dot{m}_8h_8 = \dot{m}_9h_9 + \dot{m}_{10}h_{10}$ $X_{s-CO2} = \frac{\dot{m}_{10}}{\dot{m}_8}$	$\dot{E}_D = \dot{E}_8 - \left(\dot{E}_9 + \dot{E}_{10}\right)$
Spl2	$\dot{m}_9h_9 = \dot{m}_{9a}h_{9a} + \dot{m}_{9b}h_{9b}$	$\dot{E}_D = \dot{E}_9 - \left(\dot{E}_{9a} + \dot{E}_{9b}\right)$

Table 4
Energy and exergy rate balance equations for components of the three-stage ORC.

Component	Energy rate balance	Exergy rate balance
Top ORC		
EVA	$\dot{m}_3(h_3 - h_4) = \dot{m}_{18}(h_{18} - h_{23})$	$\dot{E}_D = \left(\dot{E}_3 - \dot{E}_4\right) - \left(\dot{E}_{18} - \dot{E}_{23}\right)$
TUR	$\dot{W}_{TUR} = \dot{m}_{18}(h_{18} - h_{19})$	$\dot{E}_D = \left(\dot{E}_{18} - \dot{E}_{19}\right) - \dot{W}_{TUR}$
Pump	$\dot{W}_{PU} = \dot{m}_{22}(h_{22} - h_{21})$	$\dot{E}_D = \dot{W}_{PU} - \left(\dot{E}_{22} - \dot{E}_{21}\right)$
HEX1	$\dot{m}_{23}(h_{23} - h_{22}) = \dot{m}_{19}(h_{19} - h_{20})$ $\varepsilon_{HEX1} = \frac{T_{19} - T_{20}}{T_{19} - T_{22}}$	$\dot{E}_D = \left(\dot{E}_{19} - \dot{E}_{20}\right) - \left(\dot{E}_{23} - \dot{E}_{22}\right)$
HEX2	$\dot{m}_{20}(h_{20} - h_{21}) = \dot{m}_{30}(h_{30} - h_{29})$	$\dot{E}_D = \left(\dot{E}_{20} - \dot{E}_{21}\right) - \left(\dot{E}_{30} - \dot{E}_{29}\right)$
Middle ORC		
EVA	$\dot{m}_{36}(h_{36} - h_{37}) = \dot{m}_{24}(h_{24} - h_{30})$	$\dot{E}_D = \left(\dot{E}_{36} - \dot{E}_{37}\right) - \left(\dot{E}_{24} - \dot{E}_{30}\right)$
TUR	$\dot{W}_{TUR} = \dot{m}_{24}(h_{24} - h_{25})$	$\dot{E}_D = \left(\dot{E}_{24} - \dot{E}_{25}\right) - \dot{W}_{TUR}$
PUMP	$\dot{W}_{PU} = \dot{m}_{28}(h_{28} - h_{27})$	$\dot{E}_D = \dot{W}_{PU} - \left(\dot{E}_{28} - \dot{E}_{27}\right)$
HEX3	$\dot{m}_{25}(h_{25} - h_{26}) = \dot{m}_{28}(h_{29} - h_{28})$ $\varepsilon_{HEX3} = \frac{T_{25} - T_{26}}{T_{25} - T_{28}}$	$\dot{E}_D = \left(\dot{E}_{25} - \dot{E}_{26}\right) - \left(\dot{E}_{29} - \dot{E}_{28}\right)$
HEX4	$\dot{m}_{26}(h_{26} - h_{27}) = \dot{m}_{35}(h_{35} - h_{34})$	$\dot{E}_D = \left(\dot{E}_{25} - \dot{E}_{26}\right) - \left(\dot{E}_{29} - \dot{E}_{28}\right)$
Bottom ORC		
EVA	$\dot{m}_{37}(h_{37} - h_{38}) = \dot{m}_{31}(h_{31} - h_{35})$	$\dot{E}_D = \left(\dot{E}_{37} - \dot{E}_{38}\right) - \left(\dot{E}_{31} - \dot{E}_{35}\right)$
TUR	$\dot{W}_{TUR} = \dot{m}_{31}(h_{31} - h_{32})$	$\dot{E}_D = \left(\dot{E}_{31} - \dot{E}_{32}\right) - \dot{W}_{TUR}$
PUMP	$\dot{W}_{PU} = \dot{m}_{34}(h_{34} - h_{33})$	$\dot{E}_D = \dot{W}_{PU} - \left(\dot{E}_{34} - \dot{E}_{33}\right)$
Condenser	$\dot{m}_{32}(h_{32} - h_{35}) = \dot{m}_{39}(h_{40} - h_{36})$	$\dot{E}_D = \left(\dot{E}_{32} - \dot{E}_{33}\right) - \left(\dot{E}_{40} - \dot{E}_{39}\right)$

where a_k is the activity of species k, defined as the ratio between the vapor pressure of species k in the mixture and that of the pure species, and M_{sol} is the molecular weight of the LiBr-water solution. The rate of exergy for a stream can be defined as follows:

$$\dot{E} = \dot{E}_{ph} + \dot{E}_{ch} \tag{6}$$

The exergy equation applied to each control volume is expressed as follows and is used to evaluate the exergy destruction rate of individual components:

$$\dot{E}_{D,k} + \dot{E}_{Loss,k} = \dot{E}_{F,k} - \dot{E}_{P,k} \tag{7}$$

Here, the subscripts “D,” “F,” and “P” represent exergy destruction, fuel exergy, and product exergy, respectively.

3.1.1. *Concentrated solar power system*

The detailed methodology employed here, including the derivation of equations, is provided in the supplementary file. Solar salt has been chosen as the working fluid for the CSP subsystem. Solar salt (60 % sodium-nitrate and 40 % potassium-nitrate) is an effective heat transfer fluid and thermal energy storage medium, offering advantages such as a high thermal stability, allowing operation at temperatures up to 585 °C, and a wide operational temperature range [53]. The energy and exergy balance equations for the components of the CSP subsystem are detailed in Table 2.

3.1.2. *Supercritical CO_2 cycle subsystem*

The primary components of the s-CO_2 subsystem are compressors, recuperators, a turbine, a mixer, a cooler, a heater, and a generator. The relevant energy and exergy rate balance equations are provided in Table 3.

3.1.3. *Three-stage ORC cycle*

The three-stage ORC system consists of three top, middle and bottom ORC subsystems. Energy and exergy rate balance equations for the three-stage ORC power cycle components are given in Table 4.

3.1.4. *Multi-effect desalination system*

The system includes a mechanical vapor compressor (MVC), a pump

Table 5
Mass, energy and exergy rate balance equations for multi-effect desalination system.

Component	Mass and energy rate balance	Exergy rate balance
MVC	$\dot{W}_{MVC} = \dot{m}_{50}(h_{50} - h_{57})$	$\dot{E}_D = \dot{W}_{MVC} - \left(\dot{E}_{50} - \dot{E}_{57}\right)$
Pump	$\dot{W}_{PU} = \dot{m}_{72}(h_{73} - h_{72})$	$\dot{E}_D = \dot{W}_{PU} - \left(\dot{E}_{73} - \dot{E}_{72}\right)$
Effect-I	$\dot{m}_{50}(h_{50} - h_{65}) = \dot{m}_{51}h_{51} + \dot{m}_{58}h_{58} - \dot{m}_{43}h_{43}$ $\dot{m}_{58}X_{58} = \dot{m}_{43}X_{43}$ $\dot{m}_{50} = \dot{m}_{65},\ \dot{m}_{43} = \dot{m}_{51} + \dot{m}_{58}$	$\dot{E}_D = \left(\dot{E}_{50} - \dot{E}_{65}\right) - \left(\dot{E}_{51} + \dot{E}_{58} - \dot{E}_{43}\right)$
Effect-II	$\dot{m}_{51}(h_{51} - h_{66}) = \dot{m}_{52}h_{52} + \dot{m}_{59}h_{59} - \dot{m}_{44}h_{44} - \dot{m}_{58}h_{58}$ $\dot{m}_{59}X_{59} = \dot{m}_{44}X_{44} + \dot{m}_{58}X_{58}$ $\dot{m}_{51} = \dot{m}_{66},\ \dot{m}_{44} + \dot{m}_{58} = \dot{m}_{52} + \dot{m}_{59}$	$\dot{E}_D = \left(\dot{E}_{51} - \dot{E}_{66}\right) - \left(\dot{E}_{52} + \dot{E}_{59} - \dot{E}_{44} - \dot{E}_{58}\right)$
Effect-III	$\dot{m}_{52}(h_{52} - h_{67}) = \dot{m}_{53}h_{53} + \dot{m}_{60}h_{60} - \dot{m}_{45}h_{45} - \dot{m}_{59}h_{59}$ $\dot{m}_{60}X_{60} = \dot{m}_{45}X_{45} + \dot{m}_{59}X_{59}$ $\dot{m}_{52} = \dot{m}_{67},\ \dot{m}_{45} + \dot{m}_{59} = \dot{m}_{53} + \dot{m}_{60}$	$\dot{E}_D = \left(\dot{E}_{52} - \dot{E}_{67}\right) - \left(\dot{E}_{53} + \dot{E}_{60} - \dot{E}_{45} - \dot{E}_{59}\right)$
Effect-IV	$\dot{m}_{53}(h_{53} - h_{68}) = \dot{m}_{54}h_{54} + \dot{m}_{61}h_{61} - \dot{m}_{46}h_{46} - \dot{m}_{60}h_{60}$ $\dot{m}_{61}X_{61} = \dot{m}_{46}X_{46} + \dot{m}_{60}X_{60}$ $\dot{m}_{53} = \dot{m}_{68},\ \dot{m}_{46} + \dot{m}_{60} = \dot{m}_{54} + \dot{m}_{61}$	$\dot{E}_D = \left(\dot{E}_{53} - \dot{E}_{68}\right) - \left(\dot{E}_{54} + \dot{E}_{61} - \dot{E}_{46} - \dot{E}_{60}\right)$
Effect-V	$\dot{m}_{54}(h_{54} - h_{69}) = \dot{m}_{55}h_{55} + \dot{m}_{62}h_{62} - \dot{m}_{47}h_{47} - \dot{m}_{61}h_{61}$ $\dot{m}_{62}X_{62} = \dot{m}_{47}X_{47} + \dot{m}_{61}X_{61}$ $\dot{m}_{54} = \dot{m}_{69},\ \dot{m}_{47} + \dot{m}_{61} = \dot{m}_{55} + \dot{m}_{62}$	$\dot{E}_D = \left(\dot{E}_{54} - \dot{E}_{69}\right) - \left(\dot{E}_{55} + \dot{E}_{62} - \dot{E}_{47} - \dot{E}_{61}\right)$
Effect-VI	$\dot{m}_{55}(h_{55} - h_{70}) = \dot{m}_{56}h_{56} + \dot{m}_{63}h_{63} - \dot{m}_{48}h_{48} - \dot{m}_{62}h_{62}$ $\dot{m}_{63}X_{63} = \dot{m}_{48}X_{48} + \dot{m}_{62}X_{62}$ $\dot{m}_{55} = \dot{m}_{70},\ \dot{m}_{48} + \dot{m}_{62} = \dot{m}_{56} + \dot{m}_{63}$	$\dot{E}_D = \left(\dot{E}_{55} - \dot{E}_{70}\right) - \left(\dot{E}_{56} + \dot{E}_{63} - \dot{E}_{48} - \dot{E}_{62}\right)$
Effect-VII	$\dot{m}_{56}(h_{56} - h_{71}) = \dot{m}_{57}h_{57} + \dot{m}_{64}h_{64} - \dot{m}_{49}h_{49} - \dot{m}_{63}h_{63}$ $\dot{m}_{64}X_{64} = \dot{m}_{49}X_{49} + \dot{m}_{63}X_{63}$ $\dot{m}_{56} = \dot{m}_{71},\ \dot{m}_{49} + \dot{m}_{63} = \dot{m}_{57} + \dot{m}_{64}$	$\dot{E}_D = \left(\dot{E}_{56} - \dot{E}_{71}\right) - \left(\dot{E}_{57} + \dot{E}_{64} - \dot{E}_{49} - \dot{E}_{63}\right)$

Table 6
Description of parameters used in the proton exchange membrane electrolyzer.

Term	Equation
Nerst equation	$V_0 = 1.229 - 0.00085(T_{PEME} - 298)$
Anode over-potential equation	$V_{act,an} = \frac{RT}{F}\sin^{-1}\frac{J}{2J_{0,an}}$ $J_{0,an} = J_{an}^{ref}\exp\left(\frac{-E_{act,an}}{\overline{R}T}\right)$ $E_{act,an} = 18\,{KJ}/{mole}$
Cathode over-potential equation	$V_{act,ca} = \frac{RT}{F}\sin^{-1}\frac{J}{2J_{0,ca}}$ $J_{0,ca} = J_{ca}^{ref}\exp\left(\frac{-E_{act,ca}}{\overline{R}T}\right)$ $E_{act,ca} = 18\frac{kJ}{mole}$
Ohmic over-potential equation	$V_{ohm} = J \times R_{PEME}$ $R_{PEME} = \int_0^D \frac{dx}{\sigma_{PEME}[\lambda(x)]}$ $\sigma_{PEME}[\lambda(x)] = [0.5139\lambda(x) - 0.326]\exp\left[1268\left(\frac{1}{303} - \frac{1}{T_{PEME}}\right)\right]$

and the seven effects system. The system schematic is presented in Fig. 2. Mass, energy and exergy rate balance equations for the desalination subsystem are presented in Table 5.

3.1.5. Proton exchange membrane electrolyzer (PEME)

In an electrolysis cell, water is separated into oxygen and hydrogen using both thermal and electrical energy. During the process, hydrogen is generated at the cathode, while oxygen is produced at the anode, based on the following equation [46].

Table 7
Energy and exergy rate balance equations for components of the LiBr-water cooling system.

Component	Energy rate balance	Energy rate balance
SHE	$\dot{m}_{81}(h_{81} - h_{80}) = \dot{m}_{82}(h_{82} - h_{83})$ $\varepsilon_{SHE} = \frac{T_{82} - T_{83}}{T_{82} - T_{80}}$	$\dot{E}_D = \left(\dot{E}_{82} - \dot{E}_{83}\right) - \left(\dot{E}_{81} - \dot{E}_{80}\right)$
GEN	$\dot{m}_{9a}(h_{9a} - h_{11a}) = \dot{m}_{85}h_{85} + \dot{m}_{82}h_{82} - \dot{m}_{81}h_{81}$	$\dot{E}_D = \left(\dot{E}_{9a} - \dot{E}_{11a}\right) - \left(\dot{E}_{82} + \dot{E}_{85} - \dot{E}_{81}\right)$
ABS	$\dot{m}_{89}(h_{90} - h_{89}) = \dot{m}_{88}h_{88} + \dot{m}_{84}h_{84} - \dot{m}_{79}h_{79}$	$\dot{E}_D = \left(\dot{E}_{84} + \dot{E}_{85} - \dot{E}_{79}\right) - \dot{Q}_{ABS}\left(1 - \frac{T_0}{T_{79}}\right)$
EVA	$\dot{m}_{91}(h_{91} - h_{92}) = \dot{m}_{58}(h_{88} - h_{87})$ $\dot{Q}_{cooling} = \dot{m}_{91}(h_{91} - h_{92})$	$\dot{E}_D = \left(\dot{E}_{87} - \dot{E}_{88}\right) - \left(\dot{E}_{92} - \dot{E}_{91}\right)$
Condenser	$\dot{m}_{93}(h_{94} - h_{93}) = \dot{m}_{85}(h_{85} - h_{86})$	$\dot{E}_D = \left(\dot{E}_{85} - \dot{E}_{86}\right) - \left(\dot{E}_{94} - \dot{E}_{93}\right)$
Solution pump (SP)	$\dot{W}_{sp} = \dot{m}_{79}(h_{80} - h_{79})$	$\dot{E}_D = \dot{W}_{sp} - \left(\dot{E}_{80} - \dot{E}_{79}\right)$
THV1	$h_{84} = h_{83}$	$\dot{E}_D = \dot{E}_{83} - \dot{E}_{84}$
THV2	$h_{87} = h_{86}$	$\dot{E}_D = \dot{E}_{83} - \dot{E}_{84}$

$$H_2O \rightarrow H_2 + 0.5O_2 \tag{8}$$

As shown in Fig. 1, a PEM electrolyzer is selected for this study. Its thermochemical modeling is discussed in the following sections. The energy required for hydrogen production is provided by the following equation [46]:

$$\Delta H = \Delta G + T\Delta S \tag{9}$$

where ΔG is the Gibbs free energy and TΔS represents the required heat in J/molH_2. The total energy required corresponds to the theoretical energy needed to electrolyze water, excluding the losses typically encountered in real systems. The molar flow rate for hydrogen production is determined as follows [46]:

$$\dot{n}_{H_2,out} = \frac{J}{2F} = \dot{n}_{H_2O,react} \tag{10}$$

Here, J denotes the current density. Based on Eq. (10), the molar flow rate of oxygen produced is half that of the generated hydrogen. The molar flow rates of oxygen and water at the electrolysis outlet are determined as follows:

$$\dot{n}_{O_2,out} = \frac{J}{4F} \tag{11}$$

$$\dot{n}_{H_2O,out} = \dot{n}_{H_2O,in} - \frac{J}{2F} \tag{12}$$

The required electrical energy is calculated as follows:

$$E_{electric} = J \times V \tag{13}$$

where $E_{electric}$ is the input energy, and V is the cell potential, which can be expressed as follows [42]:

$$V = V_0 + V_{act,ca} + V_{act,an} + V_{ohm} \tag{14}$$

Here, $V_{act,ca}$, $V_{act,an}$ and V_{ohm} represent the activation overpotential of the cathode, the activation overpotentials of the anode, and the ohmic over-potential, respectively. V_0 denotes the reversible potential, which is derived from the Nernst equation. The over-potentials and Nernst

Table 8
Selected decision variables and their range of variations.

Decision variable	Range of variation
s-CO_2 turbine efficiency	$0.8 < \eta_{Tur,s-CO_2} < 0.95$
s-CO_2 split ratio (–)	$0.15 < X_{s-CO_2} < 0.35$
Main compressor pressure ratio (–)	$2.5 < PR_{MC} < 3.5$
Re-compressor pressure ratio (–)	$2.5 < PR_{RC} < 3.5$
Current density (A/m^2)	$1000 < J < 7000$
Number of PEME cells (–)	$120 < N_{Cell,PEME} < 160$
Bottom-ORC turbine efficiency	$0.8 < \eta_{Tur,Bottom-ORC} < 0.95$
Middle-ORC turbine efficiency	$0.8 < \eta_{Tur,Middle-ORC} < 0.95$
Pinch-point temperature difference of Evaporator (K)	$0 < \Delta T_{EVA} < 20$
ORC Heat-exchanger 1 efficiency	$0.6 < \varepsilon_{ORC-HEX1} < 0.9$

equations are detailed in Table 6.

3.1.6. LiBr-water absorption cooling subsystem

The comprehensive methodology, outlining the derivation of equations, is available in the supplementary file. Table 7 summarizes mass and energy rate balance equations for the components of the absorption cooling system.

3.1.7. Thermoelectric generator subsystem.

The equations for the efficiency of the thermoelectric generator (TEG) under the given operating conditions can be expressed as follows [49]:

$$\eta_{Teg} = \frac{\sqrt{1+ZT_m}-1}{\sqrt{1+ZT_m}+\frac{T_L}{T_H}} \tag{15}$$

Here, T_L and T_H denote the cold and hot side temperatures of the TEG, respectively. Also, ZT_m refers to the figure of merit, typically estimated between 0.2 and 1.6 depending on the materials used in the structure. In this study, a value of 0.8 is assumed for the figure of merit, based on baseline bismuth telluride. The Carnot efficiency is then defined as follows [49]:

$$\eta_{carnot} = \frac{T_L}{T_H} \tag{16}$$

Another way to express the TEG efficiency is as follows [49]:

$$\eta_{TEG} = \frac{\dot{W}_{TEG}}{\dot{Q}_{Elegant}} \tag{17}$$

Here, $\dot{W}_{TEG}$ represents the work output from the TEG, and $\dot{Q}_{Elegant}$ can be written as [49]:

$$\dot{Q}_{Elegant} = \dot{m}_{cooling}\left(h_{cold,in} - h_{cold,out}\right) \tag{18}$$

Here, $\dot{Q}_{Elegant}$ applies for an efficient liquid-based electricity generation apparatus, and its formulation follows the standard expression used for thermoelectric systems. Also, $\dot{m}_{cooling}$ denotes the mass flow rate on the cold side of the TEG, $h_{cold,in}$ the specific enthalpy of the incoming coolant, and $h_{cold,out}$ the specific enthalpy of the outgoing coolant from the TEG's cold side. With a reasonable approximation, the temperatures at the cold and hot side outlets can be estimated as follows [49]:

$$T_L = \frac{1}{2}\left(T_{cold,in} + T_{cold,out}\right) \tag{19}$$

$$T_H = \frac{1}{2}\left(T_{Hot,in} + T_{Hot,out}\right) \tag{20}$$

Furthermore, the energy and exergy efficiencies of the proposed polygeneration system can be expressed respectively as follows:

$$\eta_I = \frac{\dot{W}_{net} + \dot{m}_{H_2}LHV_{H_2} + \dot{Q}_{Heating} + \dot{Q}_{Cooling} + \dot{m}_{74}h_{fg,74}}{\dot{Q}_{Sun} + \dot{Q}_{Geothermal}} \tag{21}$$

$$\eta_{II} = \frac{\dot{W}_{NET} + \dot{E}_{H_2} + \dot{E}_{74} + \dot{Q}_{Cooling}\left(\frac{T_0}{T_{ref.cold}} - 1\right) + \dot{Q}_{Heating}\left(1 - \frac{T_0}{T_{ref.hot}}\right)}{\dot{Q}_{Sun}\left(1 - \frac{T_0}{T_{sun}}\right) + \left(\dot{E}_{36} - \dot{E}_{38}\right)} \tag{22}$$

where $T_{ref,cold}$ and $T_{ref,hot}$ refer to T_{92} and T_{40}, respectively.

3.2. Multi-objective optimization

Among the various multi-objective optimization methods, the Grey Wolf Optimization algorithm was selected for its reliability and effectiveness. This study focuses on optimizing thermal efficiency, exergy efficiency, and hydrogen production rate to evaluate system performance and sustainability. Given the system's complexity, including detailed thermodynamic modeling of integrated systems, forecasting, and uncertainty analysis, economic and environmental objectives are beyond the current scope and will be addressed in a planned follow-up study. Key decision variables were identified through sensitivity analysis and optimized within the ranges presented in Table 8.

3.3. Case study description and data collection

Spain, particularly the Canary Islands, stands out within the EU-28 as a prime location for geothermal direct heating systems and binary cycle electricity production, with a projected geothermal generation capacity of 610 GWt [48]. Meanwhile, the presence of advanced research infrastructures, such as the GREGOR solar telescope and the Izaña Atmospheric Research Center (IZA) in Tenerife, underscores the island's strategic importance for solar energy research and development in Spain [54]. The IZA site, part of the Baseline Surface Radiation Network (BSRN), provides accurate solar radiation datasets under various atmospheric conditions, including pristine skies and periods affected by the Saharan Air Layer. Tenerife, the largest of Spain's Canary Islands, lies between 28° 00′–28° 35′ N latitude and 16° 08′–16° 55′ W longitude. According to Fig. 3-a, the island's elevation varies significantly, from −21 m at its lowest point to 3696 m at the peak of Mount Teide, the highest point in Spain. This elevation gradient contributes to diverse microclimates and solar exposure conditions across the island [55]. Moreover, Tenerife has significant high-enthalpy geothermal potential. According to Colmenar-Santos et al. [48], geothermal reservoirs on the island reach temperatures between 170 °C and 300 °C at depths of 20–2000 m.

This study used high-pressure water a geothermal reservoir as the working fluid. The operating and design parameters used for the thermodynamic modeling of the geothermal energy source system are listed in Table 1. The IZA site (28.5°N, 16.3°W) was selected for system design, as it is a well-established reference station commonly used for calibrating and validating solar radiation models. This approach is expected to yield more reliable data with reduced uncertainty for further analysis. Solar irradiance data for this coordinate were sourced from the CAMS radiation service, which combines the McClear model with MSG satellite-derived cloud cover to provide irradiance under both clear-sky and all-sky conditions [56]. CAMS was chosen over other datasets (e.g., Solcast, SolarGIS, NSRDB, Meteonorm, HelioClim) for its real-time, location-specific data and BSRN calibration at IZA [57]. Hourly data for global horizontal irradiance (GHI), diffuse horizontal irradiance (DHI), beam horizontal irradiance (BHI), and direct normal irradiance (DNI) from 8 AM to 6 PM, spanning from January 2005 to July 2024 (Fig. 3-b) were used for solar data prediction, as well as to assess uncertainty and system sensitivity to solar variability.

3.4. Forecasting and uncertainty analysis

This research quantifies the impact of DNI uncertainty on solar energy system performance by implementing a predictive LSTM model and

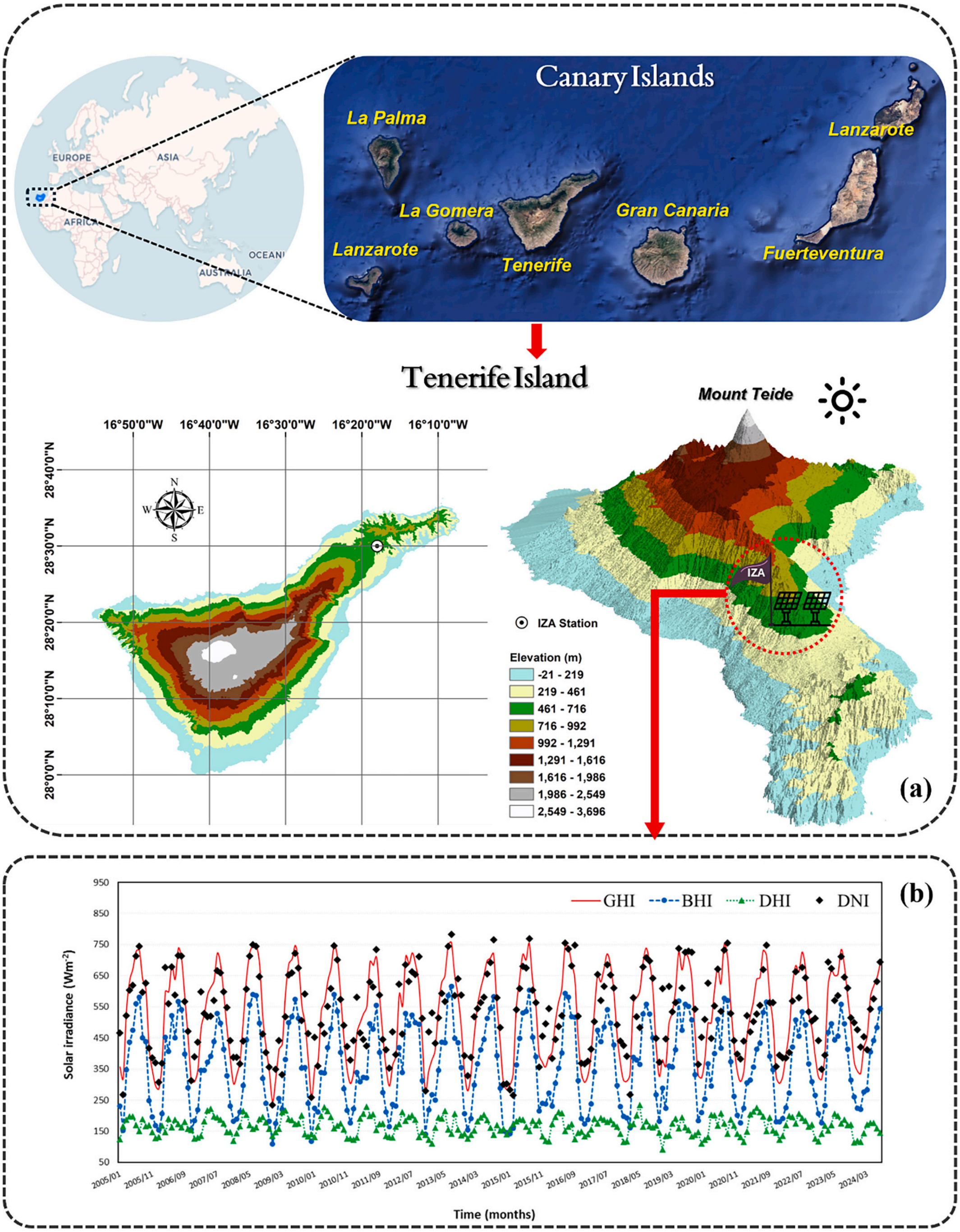

Fig. 3. (a) Geographic location and digital elevation map of Tenerife Island, with the position of the IZA station highlighted. The elevation data were derived from the NASA SRTM Digital Elevation 30 m dataset [58]; (b) Solar irradiance data for the IZA station extracted from the CAMS Radiation Service [59]. The figure illustrates the key parameters—DNI, GHI, DHI, and BHI—used for the uncertainty analysis and forecasting, covering the period January 2005 to July 2024.

Monte Carlo simulations. The LSTM model projects future DNI values based on historical data, while the Monte Carlo method facilitates an extensive uncertainty analysis by generating a range of potential outcomes from both historical and predicted data.

3.4.1. *Long-short-term memory (LSTM)-based prediction*

Conventional neural networks lack memory mechanisms, making them ineffective at modeling long-term dependencies in sequential data. Recurrent neural networks (RNNs) mitigate this by passing information through hidden states, yet still face vanishing gradient issues [60]. LSTM networks, introduced by Hochreiter and Schmidhuber [61], overcome this with memory cells and gating mechanisms (input, forget, and output), enabling them to retain information across long sequences. Their ability to learn both short- and long-term temporal patterns makes them well-suited for modeling solar irradiance time series. In this study, daily values of GHI, DHI, BHI, and DNI were used as inputs to the model, and subsequently, the monthly average DNI for July was projected for the period 2024 to 2030. The neural network architecture utilized in this research is based on the encoder-decoder or sequence-to-sequence (seq2seq) framework, as proposed by Cho et al. [62] which enables the model to handle varying input and output time steps [63]. To train the model, a sliding window technique was applied to generate input-output pairs. The performance of the LSTM model was evaluated using the coefficient of determination (DC), also referred to as the Nash-

Table 9
Fuel, product, and exergy destruction rates, along with the exergy efficiency for each component of proposed polygeneration system.

Component	$\dot{E}_{Fuel}$	$\dot{E}_{Product}$	$\dot{E}_{Destruction}$	ε (%)
CSP				
Heliostat field	49,164	29,496	19,668	52.43
Receiver	29,496	20,474	9023	69.41
Pump	1.251	1.155	0.6254	92.35
Supercritical CO_2 Power cycle				
GEN	9286	9133	152.6	98.36
TUR	10,851	10,369	482.5	95.55
HTR	7255	6675	579.8	92.01
LTR	5136	4441	695.5	86.46
MC	3183	2830	353.1	88.91
RC	2098	1926	171.6	91.82
Cooler	335.4	223.3	112	66.6
Heater	173.3	114.9	42.02	66.34
Mixer 1	26,724	26,724	0	100
Mixer 2	13,040	13,040	0	100
Splitter 1	19,290	19,290	0	100
Splitter 2	14,467	14,467	0	100
Three-stage ORC Power Cycle				
Top ORC				
EVA 1	5407	4701	705.8	86.95
TUR 1	1388	1259	128.9	90.72
Pump 1	127	111.3	15.75	87.6
HEX 1	550.7	530	20.7	96.25
HEX 2	3475	3404	71.27	97.95
Middle ORC				
EVA 2	168.1	150.3	17.81	89.41
TUR 2	1998	1782	216.3	89.17
Pump 2	35.4	29.82	5.586	84.22
HEX 3	361.2	309	52.24	85.54
HEX 4	2009	1623	385.9	80.78
Bottom ORC				
EVA 3	110.5	84.22	26.29	76.21
TUR 3	1370	1194	175.9	87.16
Pump 3	4.846	3.98	0.8656	82.14
Condenser	753.2	328.2	425	43.57
PEME				
PEM electrolyzer	1259	550.1	708.9	43.69
Multi-Effect Desalination System				
MVC	137.9	126.9	11.02	92.01
Pump	1.431	1.119	0.3118	78.22
Effect-I	650.1	638.2	11.88	98.17
Effect-II	620.5	613.2	7.291	98.82
Effect-III	598.8	591.6	7.195	98.8
Effect-IV	580.2	573	7.154	98.77
Effect-V	564.4	557.3	7.17	98.73
Effect-VI	551.3	544.1	7.247	98.69
Effect-VII	540.7	533.3	7.387	98.63
LiBr-Water Absorption Cooling System				
SHE	188.8	135.7	53.06	71.89
GEN	1303	893.9	408.8	68.62
ABS	840.8	268.8	572	31.97
EVA	250.6	116.1	134.5	46.32
Condenser	235.2	77.88	157.3	33.12
THV 1	1312	1312	0.001417	100
THV 2	7.39	7.39	0.0001701	100

Table 10
Main results of the integrated polygeneration proposed system for the baseline condition.

Parameter	Value
Overall energy efficiency (%)	62
Overall exergy efficiency (%)	17
Freshwater production rate (m^3/h)	20.7
Hydrogen production rate (kg/h)	22.6
Oxygen production rate (kg/h)	180
Heating load (kW)	6848
Cooling load (kW)	4416
Net power production rate (kW)	7844
Total exergy destruction rate (kW)	35,631

Sutcliffe efficiency, and the root mean square error (RMSE). These metrics were calculated as follows [64]:

$$\mathrm{RMSE} = \sqrt{\frac{\sum (\mathrm{X}-\mathrm{C})^2}{\mathrm{N}}}; 0 \leq RMSE < +\infty \tag{23}$$

$$\mathrm{DC} = 1 - \frac{\sum (\mathrm{X}-\mathrm{C})^2}{\sum (\mathrm{X}-\overline{\mathrm{X}})^2}; -\infty < DC \leq 1 \tag{24}$$

where X represents the DNI, C denotes the computed value by the model (here, LSTM), and $\overline{\mathrm{X}}$ denotes the average of the DNI with N values.

3.4.2. *Monte Carlo simulation*

Monte Carlo simulations, based on stochastic models and probability distributions, were used to project outcomes under DNI uncertainty. Forward uncertainty analysis was conducted by applying a Gaussian distribution to historical and predicted DNI datasets. The normal distribution was selected due to its proven effectiveness in modeling solar irradiance variability, supported by prior studies [30]. Parameters for the distribution were obtained by averaging the mean and standard deviation of data from July 2005–2024 and July 2025–2030, represented by the following mathematical expression:

$$f(x) = \frac{1}{\sigma_{ave}\sqrt{2\pi}} e^{-\frac{(x-\mu_{ave})^2}{2\sigma_{ave}^2}} \tag{25}$$

Here, $f(x)$ denotes the probability density function of the normal distribution, where x is the DNI values, μ_{ave} represents the average mean, and σ_{ave} is the average standard deviation. Note that EES and MATLAB were coupled to perform Monte Carlo simulations and uncertainty propagation through the system. To achieve this, random samples of the DNI input (X_{DNI}) were drawn from the fitted normal distribution and used as inputs in the system (S) to simulate a range of outcomes. The probabilistic system output (Y) is expressed as:

$$\mathbf{Y}_i = S\left(X_{DNI}^i, \mathbf{Z}\right) + \varepsilon_i \tag{26}$$

Here, Y_i denotes the output vector for the i-th simulation, and X_{DNI}^i represents the corresponding sampled DNI input. Also, $\mathbf{Z}$ refers to the decision variables, while $S\left(X_{DNI}^i, \mathbf{Z}\right)$ captures the deterministic system response. The error term ε_i accounts for residual uncertainties. This process is repeated 10,000 times using the Monte Carlo method, producing a distribution of outputs $\{\mathbf{Y}_1, \mathbf{Y}_2, \ldots, \mathbf{Y}_{10000}\}$. Statistical metrics like mean and standard deviation of the outputs are then estimated to reflect the influence of DNI variability. Moreover, the coefficient of variation (CV) and coefficient of range (CR) were employed to further evaluate input uncertainty and output sensitivity.

4. Results

4.1. *Validation*

As outlined above, the proposed hybrid renewable polygeneration system integrates six subsystems, including a CSP system, a s-CO_2 power cycle, a three-stage ORC, a LiBr/water absorption cooling system, a PEM electrolyzer subsystem, and a MED-MVC system. The mathematical models for all subsystems were validated against data from the literature under equivalent conditions, showing strong agreement. Detailed validation tables and a figure, for the PEM electrolyzer subsystem, are provided in the supplementary file (see Tables S1–S4 and Fig. S1).

4.2. *Energy and exergy analysis results*

The state-to-state thermodynamic properties of the polygeneration system under design conditions are detailed in the supplementary file (see Table S5). The analysis considers energy and exergy relationships, utilizes the input data provided in Table 1, and is based on the

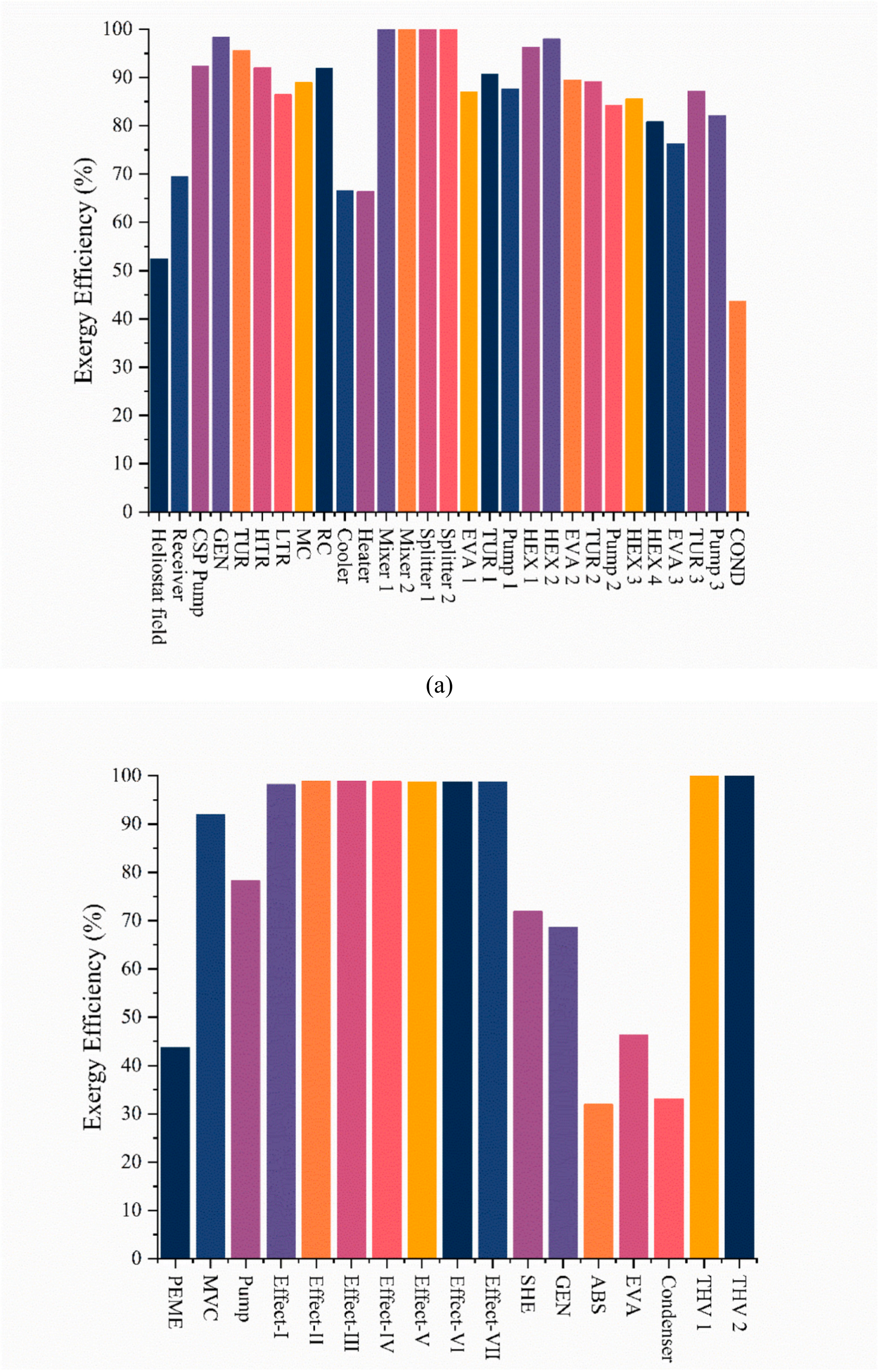

(a)

(b)

Fig. 4. Exergy efficiencies of components in the proposed system **a)** CSP, s-CO$_2$, and ORC **b)** PEME, MED-MVC, and LiBr-water absorption system.

previously stated assumptions.

Table 9 presents detailed results on the fuel exergy, product exergy and exergy destruction rates and exergy efficiencies for each component within the subsystems. In the CSP subsystem, the heliostat field exhibits a substantial exergy destruction rate (19,668 kW) and an exergy efficiency of 52.43 %, which reflects notable exergy losses during solar capture. Although the receiver operates at a higher efficiency of 69.41 %, it still experiences a considerable exergy destruction rate with a calculated value of 9023 kW. More than 80 % of the total exergy destruction rate of the system occurs in the CSP subsystem.

In the supercritical CO$_2$ power cycle, the LTR and HTR are notable for their substantial exergy destruction rates of 695.5 kW and 579.8 kW, respectively, followed by the turbine, which has an exergy destruction rate of 482.5 kW. In contrast, mixers, splitters, and the heater exhibit the lowest exergy destruction rates. When considering exergy efficiency, the generator and turbine are particularly noteworthy, achieving high efficiencies of 98.36 % and 95.55 %, respectively. However, the cooler and heater operate with lower efficiencies, around 66 %, resulting in moderate exergy destruction and indicating considerable irreversibility in the heat transfer process.

In the three-stage ORC, exergy destruction decreases across the various stages, indicating that the top cycle experiences the highest rate

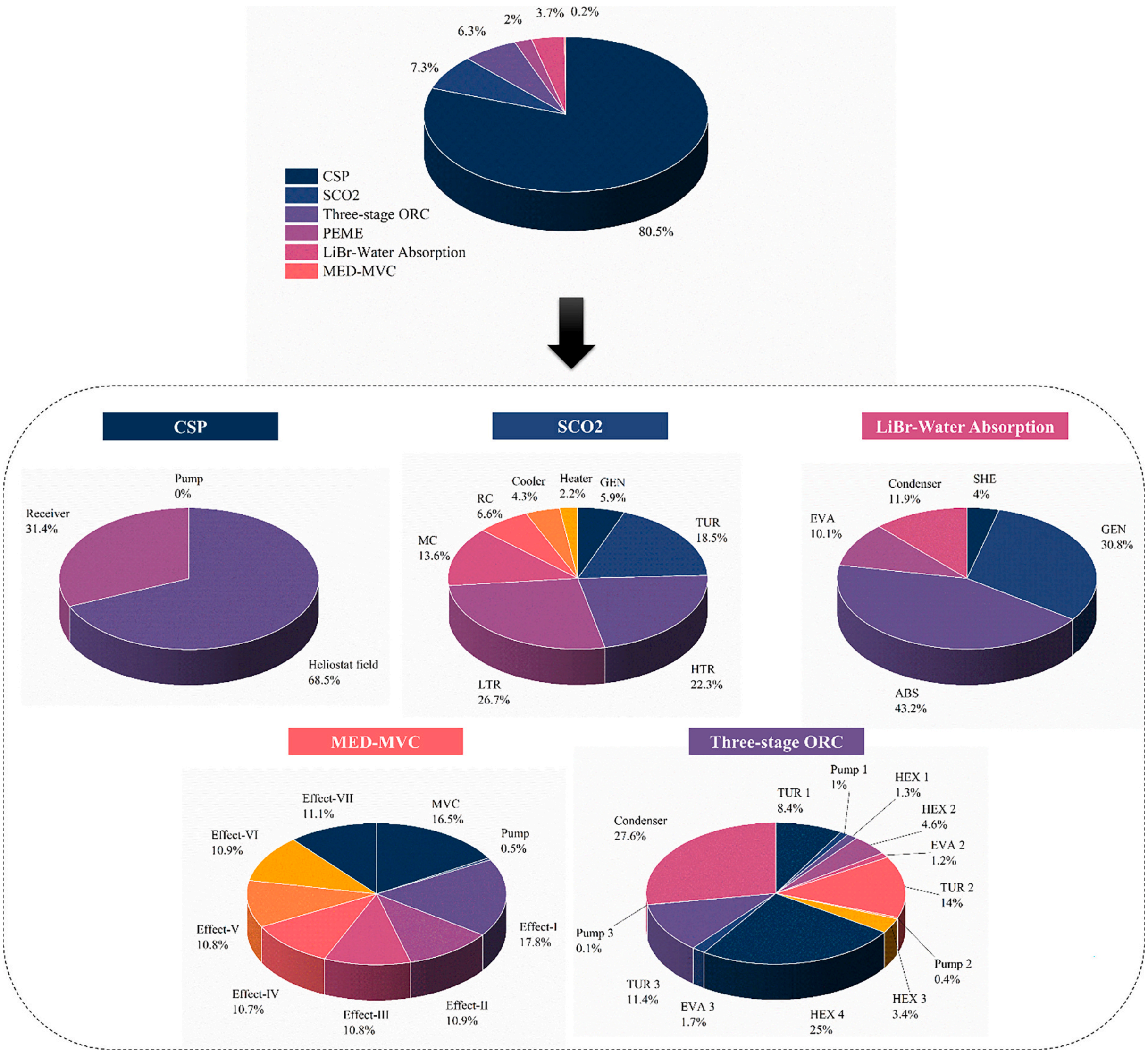

Fig. 5. Exergy destruction breakdown of subsystems and components in each subsystem.

of exergy destruction, while the bottom cycle has the lowest. Notably, the EVA 1 and the condenser exhibit the highest exergy destruction rates at 705.8 kW and 425 kW, respectively, followed closely by HEX 4, which has a rate of 385.9 kW. Conversely, the pumps and the EVA 2 demonstrate the lowest exergy destruction rates. Regarding exergy efficiency, HEX 1 and HEX 2 achieve the highest efficiencies at 96.25 % and 97.95 %, respectively, whereas the condenser has the lowest efficiency, recorded at 43.57 %.

The LiBr-water absorption cooling system has a substantial exergy destruction rate, with the ABS and GEN components exhibiting the most significant loss rates at 572 kW and 408.8 kW, respectively. Conversely, the throttling valves (THV1 and THV2) manifest the lowest exergy destruction rates and highest exergy efficiencies in the system. In contrast, the condenser and absorber components display the poorest exergy performance, with exergy efficiencies of 33.12 % and 31.97 %, respectively.

In contrast to all other subsystems, the MED-MVC system demonstrates consistently high exergy efficiencies across its operational stages, exceeding 98 %, while simultaneously exhibiting small exergy destruction rates. Furthermore, the MED-MVC subsystem contributes a mere 0.2 % to the total exergy destruction rate of the system, underscoring its superior thermodynamic performance relative to other components.

The main results for the integrated polygeneration system at the baseline condition are shown in Table 10. The overall energy and exergy efficiencies of the proposed system are found to be 62 % and 17 %, respectively. For the baseline condition, electricity, heating, cooling, hydrogen, oxygen, and freshwater are produced at the rates of 7844 kW, 6848 kW, 4416 kW, 22.6 kg/h, 180 kg/h, and 20.7 m^3/h, respectively.

Fig. 4 presents the exergy efficiencies of all system components. The throttle valves show the highest exergy efficiency, exceeding 99 %. This is because, during throttling, only the physical exergy of the stream changes, while the chemical exergy which makes up most of the total exergy remains unchanged. As a result, the overall exergy loss is very low. The effects follow with efficiencies above 98 %.In contrast, the lowest exergy efficiency is observed in the absorber of the LiBr-water subsystem at 32 %, with the condenser in the same subsystem showing the second lowest efficiency at 33.1 %.

Fig. 5 shows the exergy destruction breakdown of each subsystem and component. The CSP subsystem has the largest share at 80.5 %, followed by s-CO_2 and the three-stage ORC at 7.3 % and 6.3 %, respectively. The LiBr-water absorption cooling system accounts for 3.7 %, while the PEM electrolyzer contributes 2 %. The smallest share belongs to the MED-MVC subsystem, with just 0.2 %. In the CSP subsystem, the heliostat field and receiver dominate exergy destruction, contributing 68.5 % and 31.4 %, respectively, with the pump's share being negligible. In the s-CO_2 cycle, the LTR and HTR account for the largest

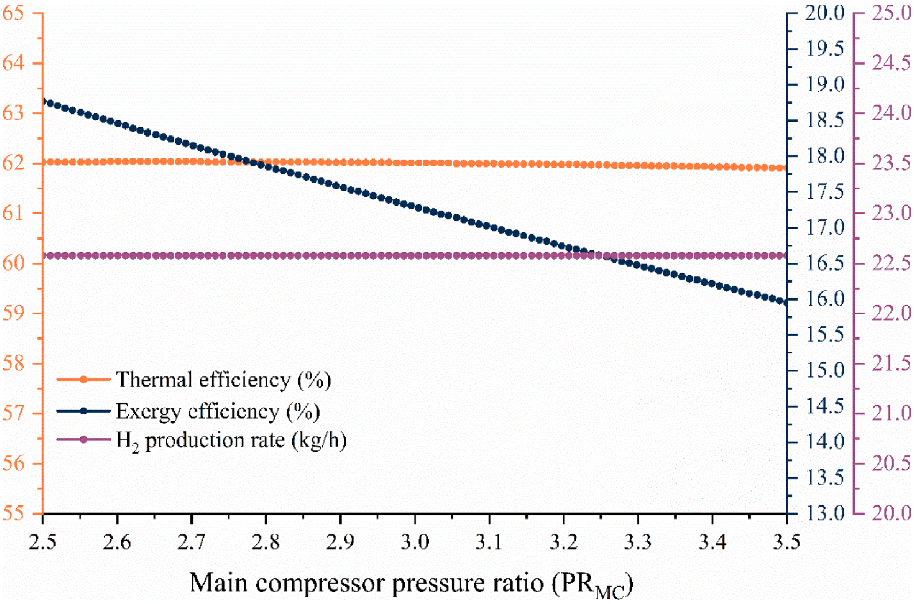

Fig. 6. Effect of main compressor pressure ratio on objective functions.

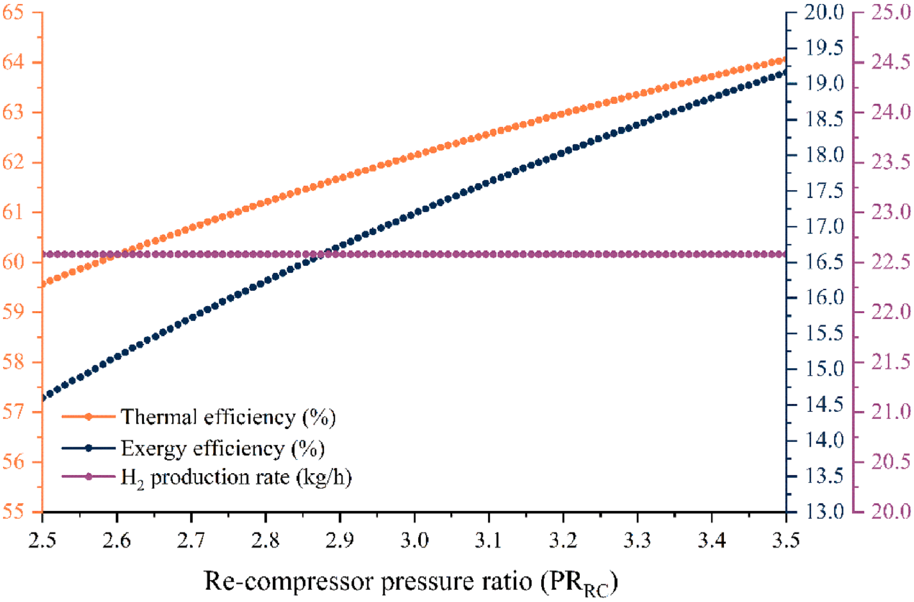

Fig. 7. Effect of re-compressor pressure ratio on objective functions.

exergy destruction shares at 26.7 % and 22.3 %, while the heater has the smallest share at 2.2 %. For the three-stage ORC, the condenser and HEX4 are the primary contributors, with 27.6 % and 25 %, respectively. In the LiBr-water absorption system, the ABS and GEN dominate, accounting for 43.2 % and 30.8 % of the exergy destruction. Finally, in the MED-MVC subsystem, Effect I and the mechanical vapor compressor contribute the most, with 17.8 % and 16.5 %, respectively.

4.3. *Sensitivity analysis*

The proposed system model includes many variables, but some are much more important and can greatly affect the system's performance. To address this, all variables were carefully analyzed using Engineering Equation Solver (EES) to identify the most effective parameters. The selected variables are presented in the Figs. 6–15.

4.3.1. *Main compressor pressure ratio*

As illustrated in Fig. 6, while the energy efficiency and hydrogen production remain nearly unchanged with the main compressor pressure ratio, the exergy efficiency declines from 18.8 % to 16 % by the end of the interval. This is due to the higher pressure ratio in the main compressor, which boosts the cooling output from 3609 kW to 4888 kW over the interval. However, it also significantly increases the power consumption of both the main compressor and the re-compressor, leading to a notable reduction in overall power production from 8668 kW to 7324 kW across the entire system.

4.3.2. *Re-compressor pressure ratio*

As depicted in Fig. 7, increasing the pressure ratio of the RC has no significant impact on hydrogen production rate but results in an increase in both energy and exergy efficiencies, which rise from 59.6 % to 64.0 % and 14.6 % to 19.2 %, respectively, within the range. This improvement

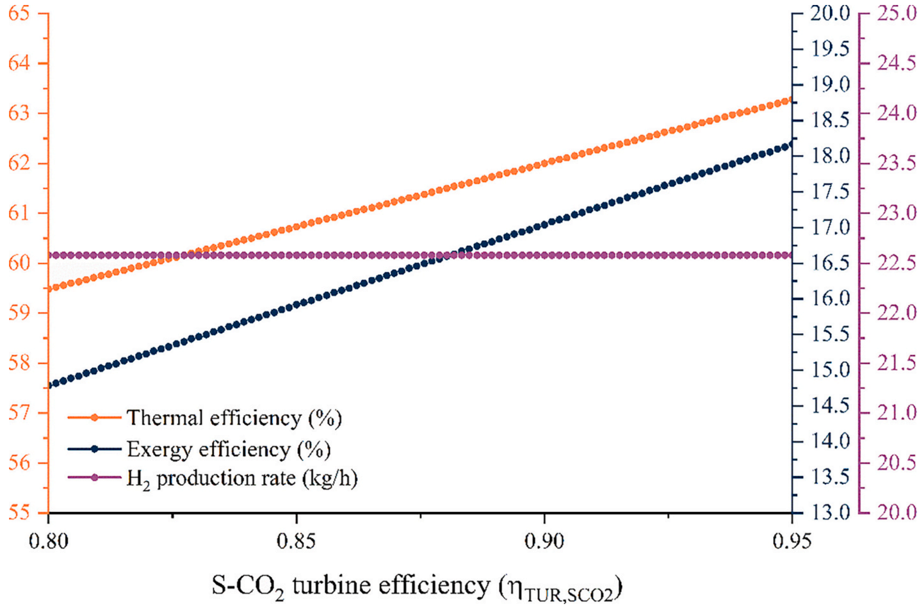

Fig. 8. Effect of s-CO_2 turbine efficiency on objective functions.

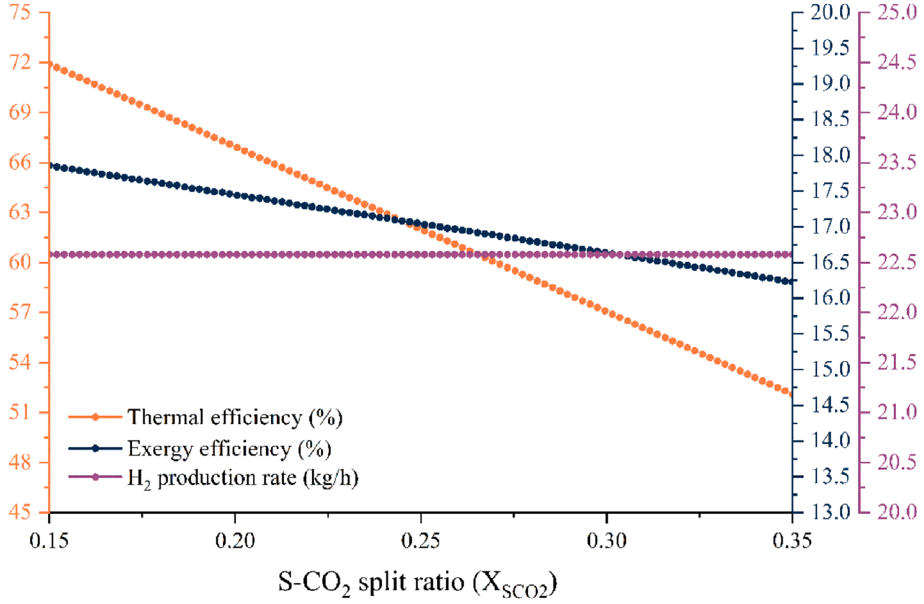

Fig. 9. Effect of s-CO_2 split ratio on objective functions.

occurs because higher pressure ratios lead to a substantial increase in the system's net power production, from 6620 kW to 8907 kW, and cooling capacity, from 4020 kW to 4797 kW, within the range. However, the power consumption of the RC also increases, from 1776 kW to 2514 kW, as re-compressor pressure ratio rises in the interval considered.

4.3.3. S-CO_2 turbine efficiency

As shown in Fig. 8, increasing the turbine isentropic efficiency decreases exergy destruction rate and enhances the power output of the s-CO_2 turbine and the cooling capacity. These values rise from 9217 kW to 10,945 kW and from 4195 kW to 4540 kW, respectively. This improvement positively influences both energy and exergy efficiencies, which increase from 59.5 % to 63.3 % and from 14.8 % to 22.3 %, respectively. However, this variation in the parameter shows no significant impact on hydrogen production rate.

4.3.4. S-CO_2 split ratio

Fig. 9 shows that increasing the split ratio $\frac{\dot{m}_{10}}{\dot{m}_8}$ leads to a decrease in both energy and exergy efficiencies, lowering them from 71.9 % to 52.1 % and 17.9 % to 16.2 %, respectively. This occurs because as the split ratio increases, the energy consumption of the RC rises significantly, from 1259 kW to 2937 kW, resulting in a substantial reduction in the system's net power production and cooling capacity, from 8242 kW to 7446 kW and 5061 kW to 3770 kW, respectively. Although the power consumption by the MC decreases throughout the range, the increase in RC energy consumption and the reduction in net power production outweigh this effect.

4.3.5. Top-ORC evaporator pinch-point difference

Fig. 10 shows that increasing the pinch point in Evaporator 1 reduces the heat transfer rate between the hot stream (molten salt) and the top ORC, resulting in a decrease in generated work from 1173 kW to 1073

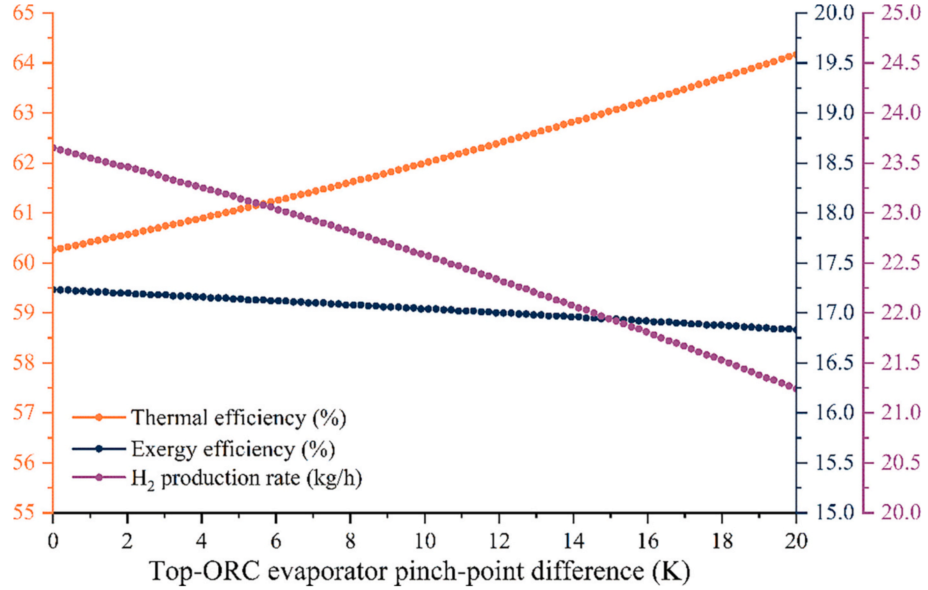

Fig. 10. Effect of top-ORC evaporator pinch-point difference on objective functions.

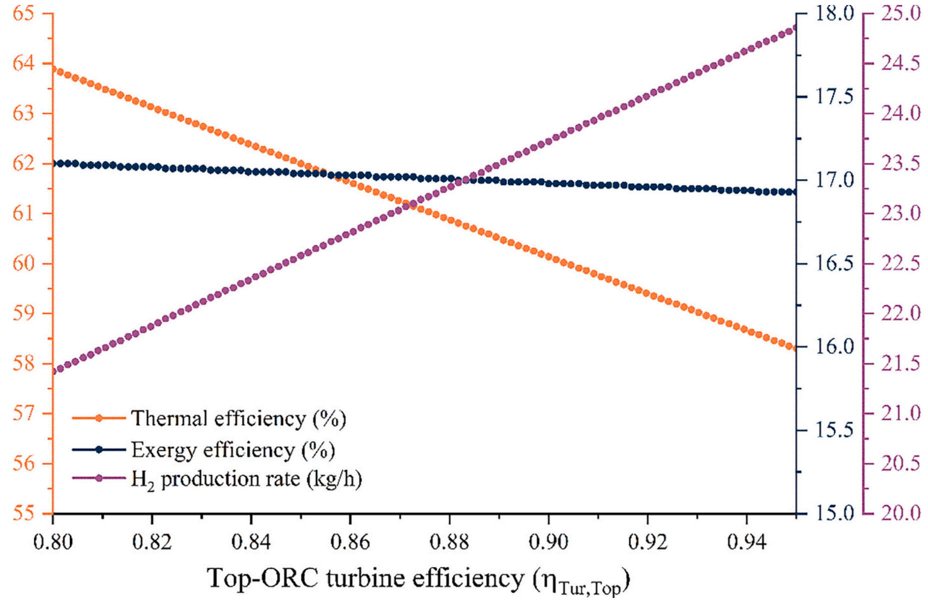

Fig. 11. Effect of top-ORC turbine efficiency on objective functions.

kW across the range. As a result, since the PEME receives its input power from the top ORC turbine, the hydrogen production rate also declines from 23.7 kg/h to 21.2 kg/h. Consequently, the exergy efficiency decreases slightly from 17.2 % to 16.8 %. However, energy efficiency increases due to the simultaneous rise in both cooling and heating outputs, which grow from 60.3 % to 64.2 % within the range.

4.3.6. *Top-ORC turbine efficiency*

Fig. 11 shows that, as all the power generated by the top ORC turbine is dedicated to the PEME for hydrogen production, an increase in turbine efficiency boosts the power output of the top ORC from 1063 kW to 1267 kW, resulting in an increase in hydrogen production rate from 21.4 kg/h to 24.9 kg/h. However, this improvement leads to reductions in both energy and exergy efficiencies due to decreases in net power production, heating, and cooling capacities under these conditions. Consequently, the energy efficiency of the proposed system decreases from 63.9 % to 58.3 %, while exergy efficiency declines slightly from 17.1 % to 16.9 % within the range.

4.3.7. *Middle-ORC turbine efficiency*

Fig. 12 illustrates that, as turbine efficiency increases, there is no significant change in energy efficiency or hydrogen production rate. However, exergy efficiency shows a slight increase, rising from 16.9 % to 17.3 % over the range. This trend occurs because improving the isentropic efficiency of the middle-ORC turbine enhances the power output of this subsystem, which in turn increases the overall net power production of the system.

4.3.8. *Bottom-ORC turbine efficiency*

Similar to the middle-ORC, Fig. 13 shows an improvement in exergy efficiency due to reduced exergy destruction, leading to increased power generation. Exergy efficiency improves slightly by 0.36 %, while energy efficiency decreases marginally by less than 0.03 % within the specified range of the bottom-ORC turbine efficiency. However, there is no

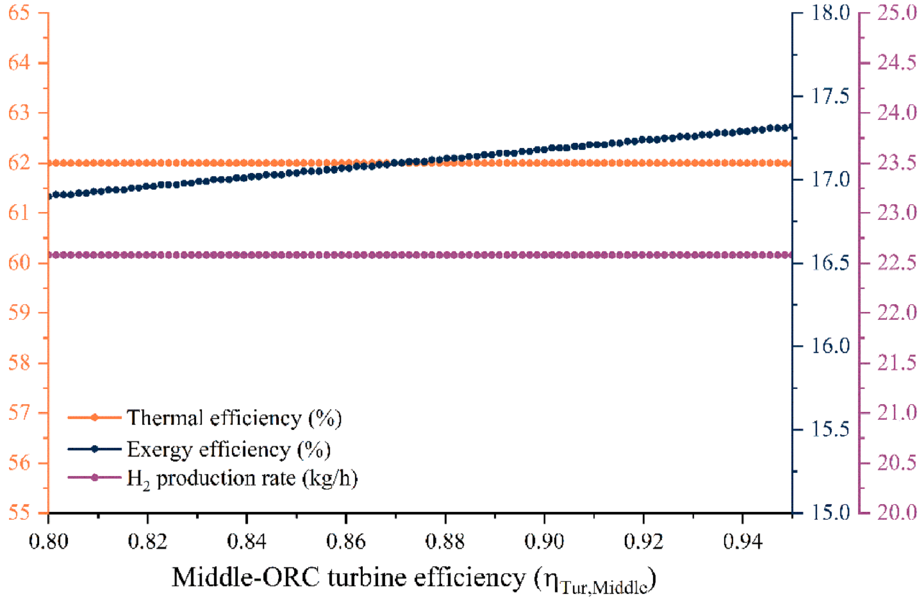

Fig. 12. Effect of middle-ORC turbine efficiency on objective functions.

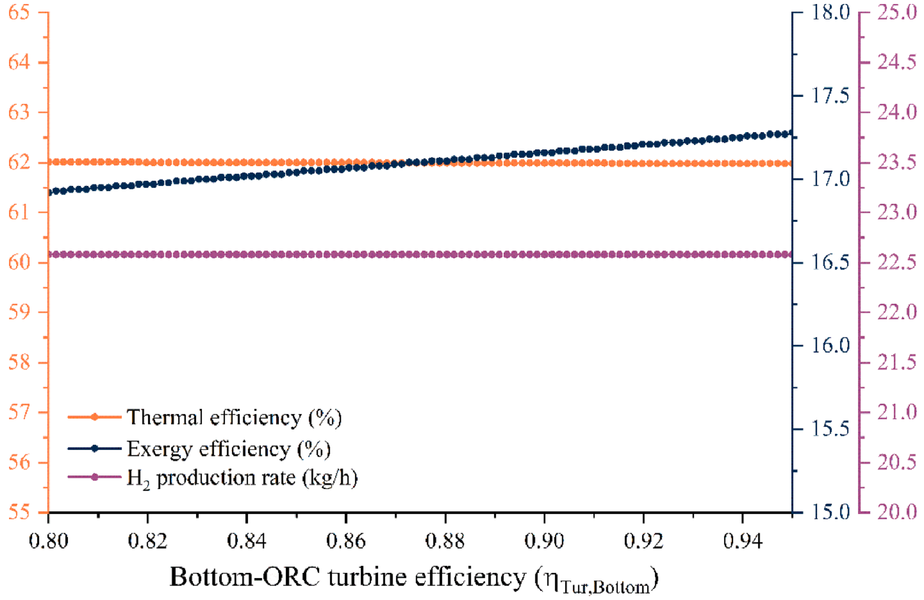

Fig. 13. Effect of bottom-ORC turbine efficiency on objective functions.

significant change in either energy efficiency or hydrogen production rate.

4.3.9. HEX 1 heat exchanger efficiency

Fig. 14 indicates that increasing the efficiency of heat exchanger 1 (HEX 1) leads to a rise in power output from the top-ORC turbine but reduces the power generated by the middle and bottom ORC turbines. Additionally, increasing the efficiency of heat exchanger 1 (increases the electricity consumption of the PEME component, resulting in a net decrease in overall power production within the system. Consequently, both energy efficiency and exergy efficiency decline, from 17.07 % to 16.99 % and 62.7 % to 60.6 %, respectively. However, the hydrogen production rate increases by 1.6 kg/h over the specified range.

4.3.10. PEME cell number

Fig. 15 illustrates that as the number of PEME cells increases, the hydrogen production rate rises by 0.3 kg/h. However, this also results in higher power consumption and reduced cooling capacity, causing energy efficiency to decline from 67.3 % to 56.7 %. Similarly, exergy efficiency experiences a slight decrease of 0.06 % due to the increased exergy destruction rate associated with the addition of more PEME cells.

4.4. Multi-objective optimization

The sensitivity analysis revealed that multiple factors significantly influence each performance metric. Consequently, to determine the optimal technical design, a tri-objective optimization approach was employed. The proposed system was optimized using the grey-wolf optimization algorithm, focusing on three objective functions: energy efficiency, exergy efficiency, and hydrogen production rate. The goal was to maximize all three objectives and identify an optimal point. It is worth noting that this process involved coupling Engineering Equation

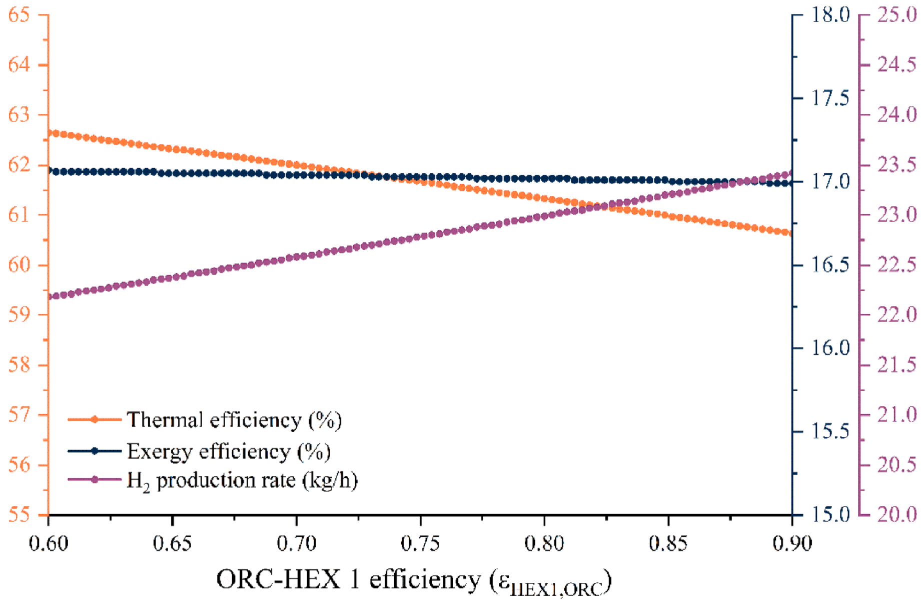

Fig. 14. Effect of ORC-HEX 1 efficiency on objective functions.

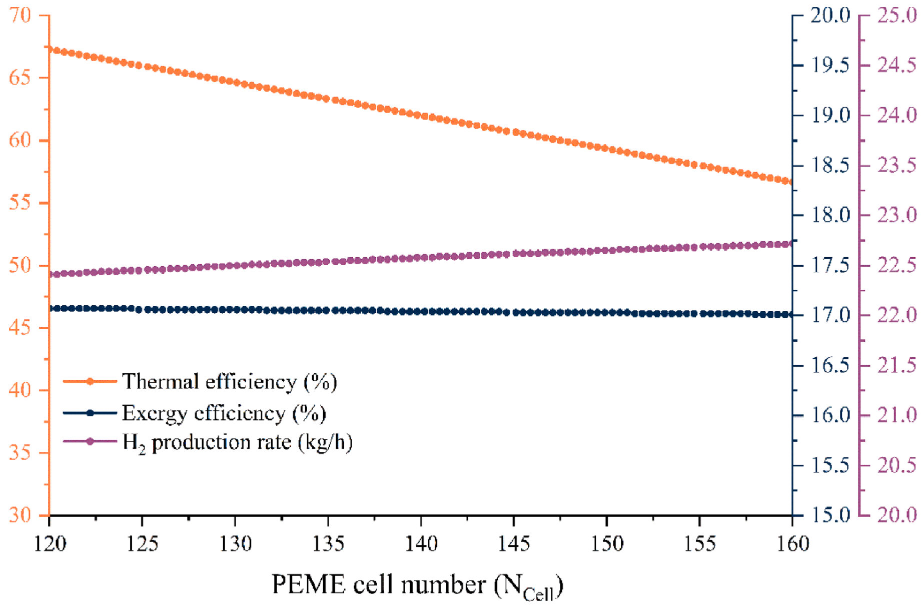

Fig. 15. Effect of PEME cell number on objective functions.

Solver (EES) with MATLAB software. This section presents the results of the multi-objective optimization of the proposed system.

Fig. 16 presents the Pareto front obtained from the grey-wolf optimization applied to the system. Each point on the Pareto front represents an optimal solution from a specific perspective. However, one point stands out as the most suitable, as it aligns best with the given conditions and scenario. The scenario focuses on maintaining high first and second efficiencies while ensuring the system's sustainability by producing sufficient hydrogen. The optimized configuration achieved energy and exergy efficiencies of 75.2 % and 23.5 %, respectively, reflecting improvements of 21 % and 38 % over the baseline condition. Additionally, the optimization outcomes showed a 18 % rise in the hydrogen production rate, along with an 8.6 % decrease in the total exergy destruction rate compared to the initial design parameters. This dual benefit indicates that the optimization not only increased the system's productive output but also reduced irreversibilities, leading to more effective resource utilization. Table 11 offers a detailed comparison of the optimized polygeneration system's performance metrics against the baseline design conditions. According to Table 11, the net power output, cooling load, freshwater production rate, and oxygen production rate improved by 40.7 %, 9.13 %, 27.6 %, and 18 %, respectively, while heating capacity decreased by 5.05 %.

4.5. DNI prediction and system performance analysis

4.5.1. DNI prediction using seq2seq LSTM-based model

In this study, a seq2seq LSTM-based model was developed to predict daily DNI for the period 2024 to 2030 at the IZA station, located in the Tenerife Island. Daily predictions were aggregated to a monthly scale, with the study focusing on the July monthly averages, as DNI typically reaches its peak during this month (see Fig. 17). The training methodology involved progressively calibrating the LSTM network using

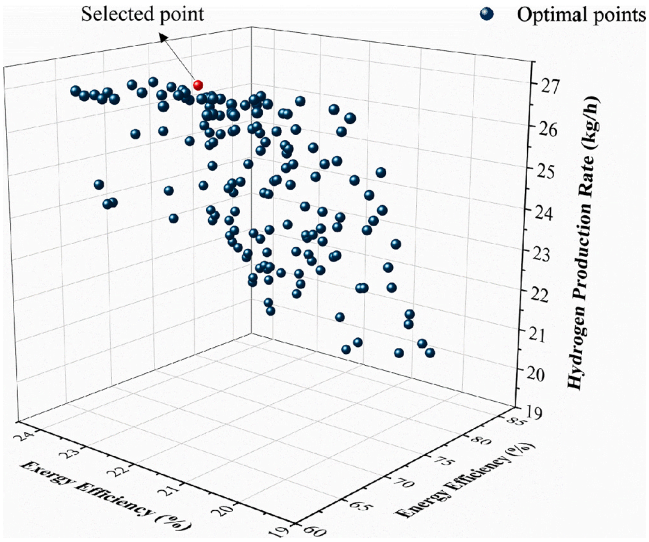

Fig. 16. Pareto optimal solutions resulting from the multi-objective optimization.

Table 11
Comparison of the results obtained after optimization and under baseline condition for the proposed system.

Parameter criteria	Baseline	Optimal point	Difference
Overall energy efficiency (%)	62	75.2	+21 %
Overall exergy efficiency (%)	17	23.5	+38 %
Rate of freshwater production (m^3/h)	20.7	26.3	+27.6 %
Rate of hydrogen production (kg/h)	22.6	26.6	+18 %
Rate of oxygen production (kg/h)	180	213	+18 %
Heating load (kW)	6848	6502	−5.05 %
Cooling load (kW)	4416	4819	+9.13 %
Net power production rate (kW)	7844	11,039	+40.7 %
Total exergy destruction rate (kW)	35,631	32,575	−8.6 %

historical data to forecast future values. Specifically, the model was trained on sequential windows (e.g., 2005–2011 to predict 2011–2017), enabling the capture of both short- and long-term temporal dependencies. This approach allowed the model to develop a robust understanding of the temporal patterns in DNI, improving its forecasting capability for the target period of 2024–2030. Although the model leveraged the entire 19-year dataset (2005–2024) for pattern recognition, recent data (2018–2024) was important for fine-tuning the model to account for recent trends and anomalies. This ensures a more accurate and reliable forecast for the future period. For each training iteration, the data was divided into calibration and validation sets, with 75 % of the data allocated for calibration and 25 % for validation. Fig. 17 presents the time series of DNI from 2005 to 2030, highlighting the LSTM model's predicted DNI values for the 2024–2030 period (shaded area). The larger yellow dots in Fig. 17a represent the July averages, highlighting that most of the maximum DNI values occur during this month. Additionally, scatterplots for the calibration and validation phases (2018–2024) are provided, demonstrating the model's performance.

As illustrated in Fig. 17, the seq2seq LSTM-based model achieved a DC of 0.72 during the calibration phase and 0.70 during the validation phase. Additionally, the model exhibited a RMSE of 140.02 W/m^2 for calibration and 78.19 W/m^2 for validation. These performance metrics demonstrate the robustness of the LSTM model in predicting DNI values. By training the LSTM model on smaller time intervals (e.g., 2005–2011 to predict 2011–2017), the seq2seq architecture was able to capture temporal dependencies over various timescales. This iterative training process enhances the model's ability to generalize and predict future values (2024–2030) with greater accuracy. DNI is affected by atmospheric conditions, cloud cover, and other environmental factors that exhibit both seasonal and multi-year trends. The inclusion of a long historical dataset enabled the model to effectively capture these periodic variations. Standard machine learning models, such as traditional LSTM, often struggle to maintain the sequence relationship between input and output over longer timeframes [63]. While regular LSTM models process time-series inputs, they predict outputs without fully accounting for temporal dependencies in the output sequence [65,66], leading to increased bias and reduced performance over extended time steps. However, by adding an extra LSTM decoder layer to handle the output as a sequence, the final LSTM-seq2seq model achieved notable improvements in statistical performance, resulting in more precise and dependable predictions. Furthermore, the predicted DNI values (Fig. 17a) exhibited trends and patterns closely aligned with the observed historical data, indicating that the seq2seq LSTM-based model effectively captured the underlying temporal dynamics of DNI, leading to reliable and accurate future predictions.

4.5.2. *System performance analysis under historical and predicted DNI values*

This section examines the performance of the proposed system under historical and predicted DNI conditions in the optimal condition. The system's key metrics, such as net power production rate, overall energy and exergy efficiency of the system, hydrogen production rate, oxygen production rate, fresh-water production rate, heating capacity, cooling load and total exergy destruction rate, are evaluated using historical average July DNI data from 2005 to 2024 and used to predict average July DNI values for 2024 to 2030. The results are presented in a Fig. 18, which illustrates the temporal variations in these metrics under both historical and predicted DNI scenarios. This analysis provides insights into the system's potential performance over time, highlighting the impact of changing solar irradiance conditions.

4.6. *Estimation of DNI uncertainty for proposed system under optimal condition*

The probabilistic characterization of DNI variability was derived through a statistical analysis of historical and predicted July DNI measurements. Employing a parametric normal distribution model ($\mu = 711.3$ kW/m^2, $\sigma = 37.6$ kW/m^2), Monte Carlo simulations were conducted comprising 10,000 iterations to propagate DNI uncertainty quantitatively (Fig. 19). The simulation output, represented by the 95 % prediction uncertainty (95PPU) in Fig. 20, comprehensively describes the potential systemic response under stochastic DNI conditions.

From the results presented in Table 12, the system outputs exhibit distinct central tendencies and variabilities. $\dot{W}_{net}$ has a mean value of 11,319.28 kW with a standard deviation of 497.73 kW, indicating moderate variability. Similarly, $\dot{Q}_{Cooling}$ and $\dot{Q}_{DWH}$ show mean values of 4944.02 kW and 6654.72 kW, respectively, accompanied by standard deviations of 222.37 kW and 271.44 kW. Among the outputs, η_I and η_{II} exhibit the lowest standard deviations (0.07 and 0.02, respectively), signifying high consistency. In contrast, $\dot{Ex}_{D,total}$ and $\dot{W}_{net}$ display the highest standard deviations (1492.61 kW and 497.73 kW, respectively). Statistical analysis revealed predominantly symmetrical distributions characterized by near-zero skewness values, demonstrating balanced variations around the central tendency. The corresponding kurtosis values, ranging between 2.41 and 2.45, indicate mesokurtic distributions, suggesting a statistically stable system with a consistent probability of observing moderate deviations under stochastic DNI conditions.

To quantitatively evaluate the sensitivity of system outputs to DNI variability, we employed the CV and CR metrics. These statistical indicators systematically measure the relative dispersion and range of each output's distribution, facilitating a comprehensive sensitivity ranking. $\dot{Q}_{cooling}$, $\dot{Ex}_{D_{total}}$, and $\dot{W}_{net}$ emerged as the most sensitive parameters, exhibiting CV values of 4.50 %, 4.47 %, and 4.40 % and

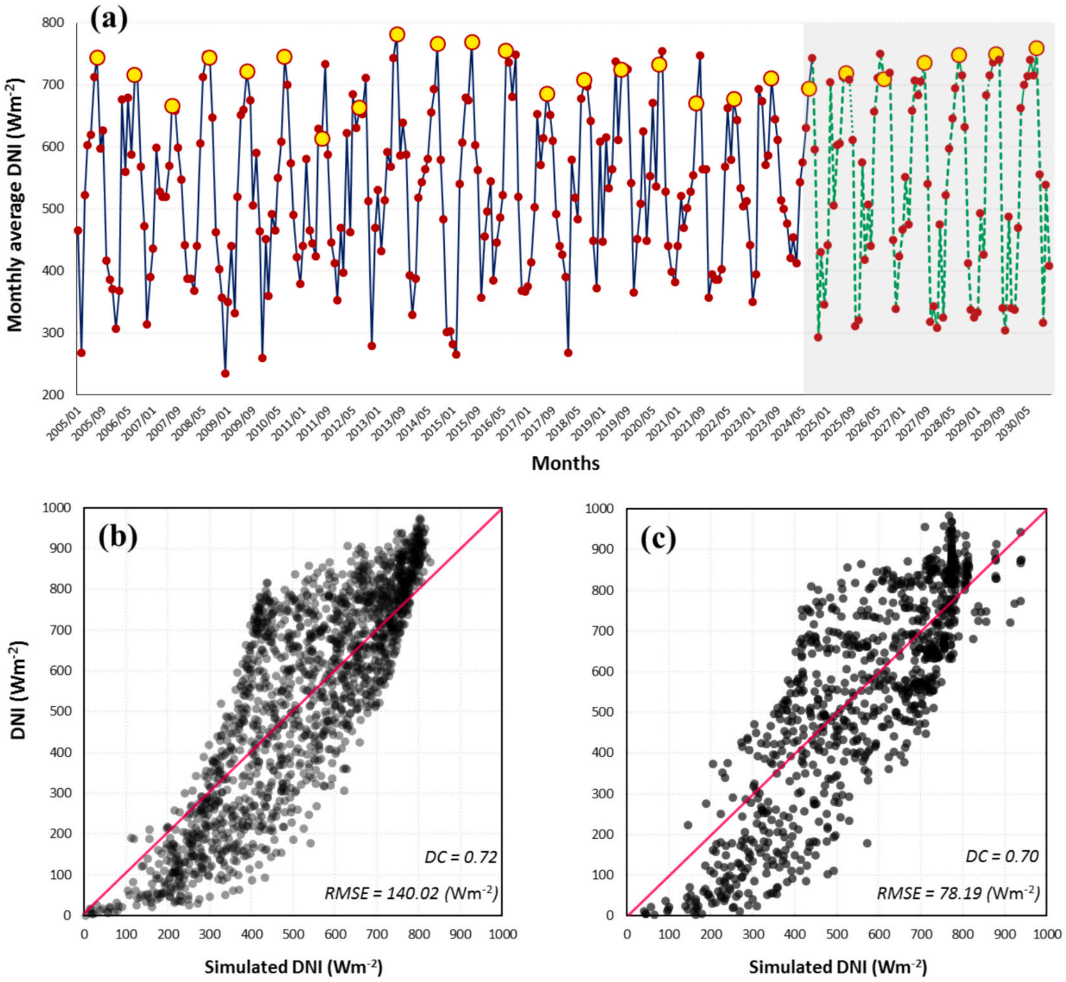

Fig. 17. (a) Time series of monthly average DNI from 2005 to 2030, with the shaded region indicating the predicted period 2024 to 2030. (b) Scatterplot showing the correlation between observed and predicted DNI values during the calibration phase (2005–2017). (c) Scatterplot for the validation phase (2018–2024), demonstrating the model's predictive performance using the LSTM model.

corresponding CR values of 10.26 %, 10.19 %, and 10.03 %. Conversely, η_I and η_{II} demonstrated strong resilience, with CV values consistently below 0.10 % and CR values of 0.20 % and 0.16 %, respectively, indicating their good stability under solar irradiance fluctuations. The higher sensitivity of $\dot{Q}_{cooling}$, $\dot{E}x_{D_{total}}$, and $\dot{W}_{net}$ to DNI variability can be attributed to their direct dependence on solar irradiance levels. Cooling systems often require substantial thermal energy, which is directly influenced by DNI fluctuations. Similarly, total exergy destruction rate is closely tied to system inefficiencies, which are exacerbated under conditions of high DNI variability. In contrast, the relatively low sensitivity of η_I and η_{II} suggests that efficiency metrics are more resilient to input variability due to their dependence on ratios rather than absolute values. Therefore, efficiency parameters exhibit lower sensitivity to fluctuating environmental conditions.

In summary, the results underscore the need for robust design considerations when optimizing solar-based systems. Outputs with higher sensitivity, such as cooling production capacity and exergy destruction rates, require careful calibration and adaptive control strategies to mitigate the impact of DNI uncertainty. On the other hand, the stability of efficiency metrics highlights their reliability as performance indicators even under variable conditions. These insights contribute to the development of resilient and adaptive energy systems designed to withstand the inherent variability of solar resources.

4.7. Comparison of performance results of proposed system with previous research

As shown in Table 13, a comprehensive comparison is conducted between several closely related and valuable case studies to facilitate an improved evaluation of the current system relative to others. The referenced case studies primarily utilize solar, geothermal, and biomass resources. By integrating efficient subsystems, maximizing waste energy recovery, and simultaneously producing five distinct outputs (power, heating, cooling, hydrogen, and freshwater), the current study achieves higher overall energy efficiency and generally higher exergy efficiency compared to similar studies, all while maintaining zero-emission (green) operations. Given the intermittent nature of renewable energy sources, dynamic system assessment is essential. Unlike comparable studies that focus solely on seasonal performance, this research conducts a dynamic analysis using both historical and forecasted data extending to 2030. The integration of machine learning to predict key operational parameters based on reliable historical data represents a distinct and novel contribution of this study. Considering the inherent intermittency of renewable energy sources, uncertainty analysis significantly enhances system reliability. This aspect is specifically addressed in the present study, distinguishing it from earlier works. However, since this study primarily emphasizes comprehensive performance enhancement, sustainability, reliability, and forecasting, aspects such as economic analysis and detailed environmental impact assessment are beyond its current scope. These important elements will be thoroughly examined in

Fig. 18. Temporal variations in the proposed system's performance metrics under historical average July DNI conditions (2005–2024) and predicted average July DNI conditions (2024–2030) under the optimal condition: a) Energy efficiency, exergy efficiency, and hydrogen production rate; b) cooling and heating loads; c) net power production and total exergy destruction rates.

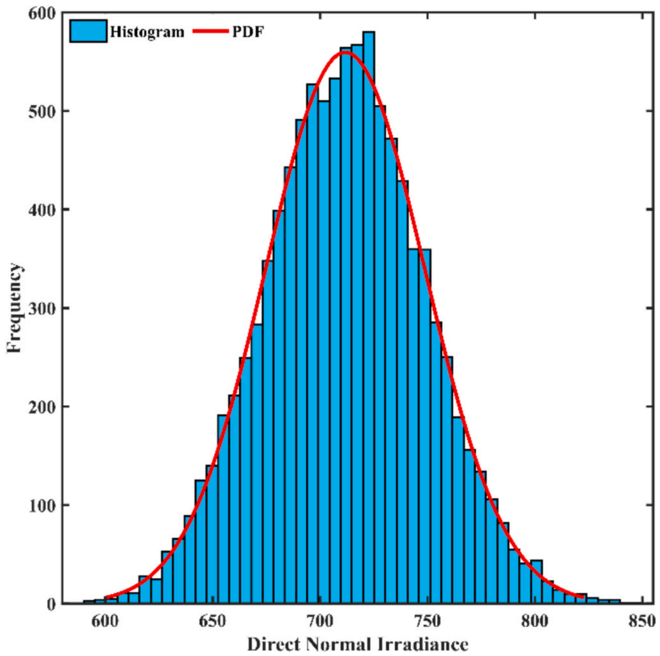

Fig. 19. Fitted probability density function for historical and predicted DNI.

a follow-up investigation.

5. Conclusion

This study has successfully designed and analyzed a novel hybrid renewable-based polygeneration system, integrating CSP, geothermal energy, a supercritical CO_2 cycle, a lithium bromide-water absorption cooling system, MED-MVC, a three-stage ORC, and a PEM electrolyzer. This innovative system enables the simultaneous production of power, heating, cooling, freshwater, and hydrogen. Through comprehensive energy and exergy analyses, we have thoroughly evaluated its performance. Utilizing the grey-wolf optimization algorithm, we optimized the system's parameters to achieve optimal efficiency. DNI data was extracted from the CAMS radiation service from 2005 to 2024, and future values were predicted from 2024 to 2030 using the seq2seq LSTM method. Furthermore, an uncertainty analysis was conducted using the Monte Carlo method to assess the impact of DNI variations on the system's performance over this period. The key findings of this study, summarized below, highlight the critical insights gained from this comprehensive investigation:

- The results show that the proposed system achieves an overall energy efficiency of 62 % and an exergy efficiency of 17 % under baseline conditions.
- In the baseline condition, the proposed system demonstrates the ability to generate a net power output of 7844 kW, provide a heating capacity of 6848 kW, handle a cooling load of 4416 kW, and produce hydrogen and oxygen at rates of 22.6 kg/h and 180 kg/h, respectively, while also producing freshwater at a rate of 20.7 kg/m^3.
- The exergy analysis revealed that the total irreversibilities within the system equaled 35,631 kW. Notably, the CSP subsystem was the primary contributor to these irreversibilities, accounting for approximately 80.5 % of the total. The s-CO_2 cycle followed with a share of 7.3 %, while the MED-MVC desalination unit had the smallest contribution at 0.2 %.
- The exergy analysis reveals that the heliostat field and receiver have the highest exergy destruction rates, at 19668 kW and 9023 kW, respectively, while pumps, mixers, and splitters exhibit the lowest. Throttle valves achieve the highest exergy efficiency, exceeding 99

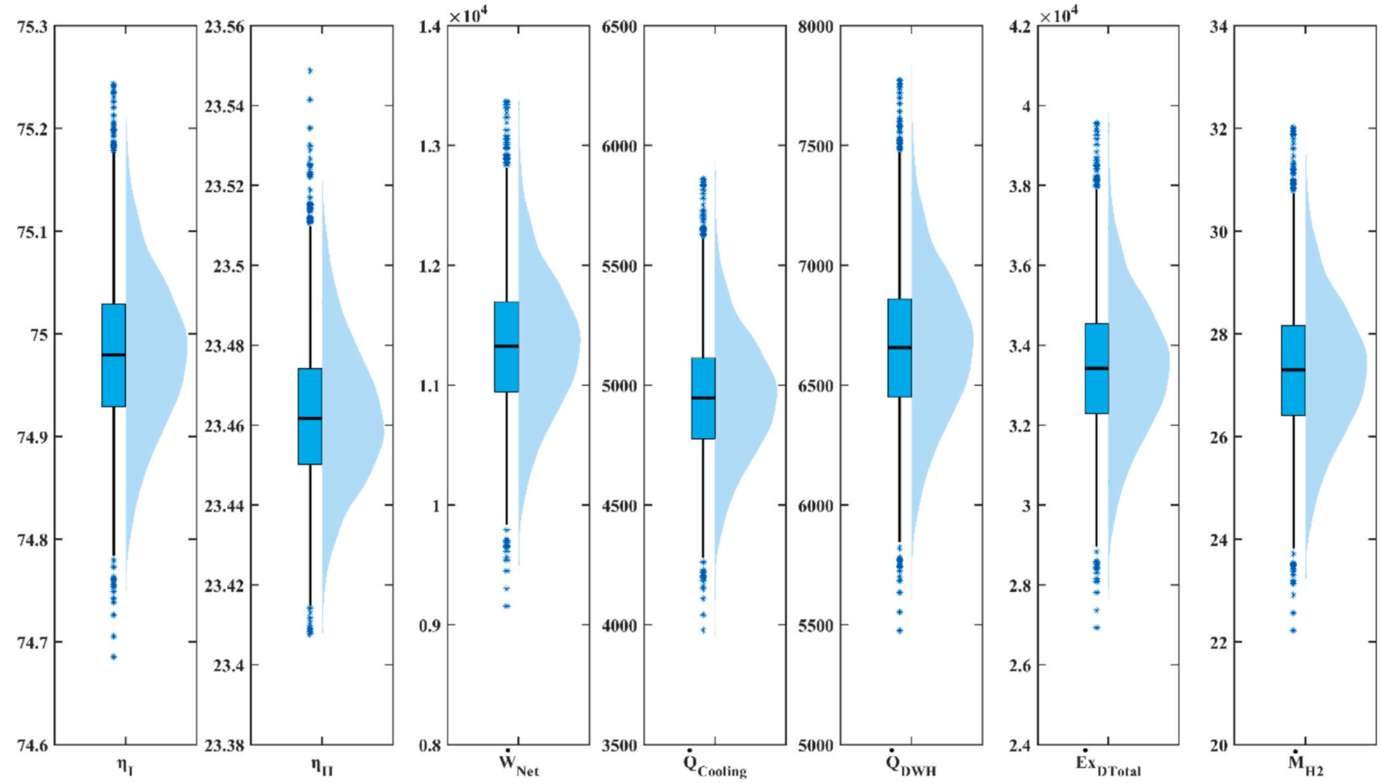

Fig. 20. 95 % confidence intervals of system outputs, including energy efficiency (η_I), exergy efficiency (η_{II}), net produced power ($\dot{W}_{net}$), cooling production capacity ($\dot{Q}_{Cooling}$), heating production capacity ($\dot{Q}_{DWH}$), total exergy destruction rate ($\dot{E}x_{D,total}$), and hydrogen production mass flow rate ($\dot{m}_{H2}$). The figure illustrates the variability of each output under DNI uncertainty, as estimated by Monte Carlo simulations.

Table 12
Descriptive statistics of input (DNI) and outputs from the Monte Carlo simulation at the optimal point.

Descriptive statistics	DNI (W/m^2)	Monte Carlo simulation of optimal point						
		η_I (%)	η_{II} (%)	$\dot{W}_{net}$ (kW)	$\dot{Q}_{cooling}$ (kW)	$\dot{Q}_{DWH}$ (kW)	$\dot{E}x_{D_{total}}$ (kW)	$\dot{M}_{H_2}\left(\frac{kg}{h}\right)$
Mean	711.3	74.98	23.46	11,319.28	4944.02	6654.72	33,414.45	27.28
SD	37.6	0.07	0.02	497.73	222.37	271.44	1492.61	1.16
Skewness	0.038	−0.02	0.20	0.01	0.01	0.01	0.01	0.00
Kurtosis	2.99	2.41	2.45	2.41	2.41	2.41	2.41	2.41
Minimum	670.5	74.83	23.43	10,190.62	4439.90	6039.21	30,030.05	24.66
Maximum	792	75.13	23.50	12,462.87	5455.07	7278.38	36,844.12	29.93
Confidence − 95 %	626.6	74.83	23.43	10,189.95	4439.60	6038.85	30,028.05	24.65
Confidence + 95 %	800.1	75.13	23.50	12,464.86	5455.96	7279.46	36,850.09	29.94
CV (%)	5.24	0.09	0.07	4.40	4.50	4.08	4.47	4.24
CR (%)	19.44	0.20	0.16	10.03	10.26	9.30	10.19	9.67
Rank		6	7	3	1	5	2	4

%, followed by effects with efficiencies above 98 %. Conversely, the absorber and condenser in the LiBr-water subsystem have the lowest efficiencies, at 31.97 % and 33.12 %, respectively.

- The optimization process resulted in significant improvements in energy and exergy efficiencies, increasing from 62 % to 75.2 % and from 17 % to 23.5 %, respectively, and also led to a 18 % increase in hydrogen production.
- The optimized system demonstrated substantial enhancements in other outputs, including a 40.7 % increase in net power production, a 27.6 % rise in freshwater production, a 9.13 % increase in cooling load, and a 18 % boost in oxygen production, while reducing total exergy destruction by 8.6 % and decreasing heating capacity by 5.05 %.
- The uncertainty analysis reveals that cooling load, total exergy destruction, and net power production are the most sensitive system outputs to DNI variability, with CV values of 4.50 %, 4.47 %, and 4.40 %, and CR values of 10.26 %, 10.19 %, and 10.03 %, respectively. This sensitivity is attributed to their direct dependence on solar irradiance levels. In contrast, energy and exergy efficiencies show minimal sensitivity to DNI fluctuations, with CV and CR values remaining below 0.10 % and 0.20 %. This resilience is likely due to their dependence on ratios rather than absolute values, which makes them more stable under varying environmental conditions.

The analysis demonstrates that large-scale, efficient, and sustainable production of power, heating, cooling, freshwater, and hydrogen is achievable through this hybrid renewable-based polygeneration system. The system's competitiveness stems from its optimized energy and exergy efficiencies, particularly through the integration of diverse renewable energy sources and advanced optimization techniques. These

Table 13
Comparison of performance results of the proposed system with previous research.

Ref.	Year	Resources	Production	Subsystems	Analysis	Energy efficiency (%)	Exergy efficiency (%)	Power (kW)/ Heating (kW)/ Cooling (kW)/ Freshwater (m^3/h)/ Hydrogen (kg/ h)	Dynamic analysis/ Forecast/ Uncertainty analysis/ Zero emission
Present study	2025	Solar Geothermal	Power Heating Cooling Freshwater Hydrogen	CSP Geothermal SCO_2 LiBr/water cooling 3-Stage ORC MED-MVC PEME TEG	Energy Exergy Sensitivity GW multi-objective optimization ML LSTM Forecasting Dynamic analysis (2005–2030) Monte Carlo Uncertainty	75.2	23.5	11,000/ 6500/ 4800/ 26.3 / 26.6	✓/✓/✓/✓
Mousavi Rabeti et al. [67]	2025	Solar Biomass	Power Freshwater	Brayton Rankine ORC Solar tower Gasification CO_2 capture MD-MED RO	Energy Exergy Exergoeconomic Techno-economic Exergoenvironment ML-based multi-objective optimization Dynamic analysis	39.82	9.1	15,500/ - / - / 98 / - /	✓/×/×/×
F. Yilamaz & B. Jamil [68]	2025	Solar	Power Heating Freshwater	CSP GT SRC ORC RO	Energy Exergy Parametric study environmental Dynamic analysis	25.1	18	3750 / 870 / - / 33.5 / - /	✓/×/×/✓
L. Zhao et al. [69]	2024	Solar Geothermal	Power Cooling Freshwater	Solar tower Geothermal LiBr/water cooling ORC HDH	Energy Exergy Economic Environmental PSO optimization Dynamic analysis	–	16	800 / - / 1350 / 28.6 / - /	✓/×/×/✓
Y. Cao et al. [70]	2022	Solar Geothermal	Power Cooling Freshwater Hydrogen	Solar collector Geothermal cycle Transcritical CO_2 cycle HDH PEME	Energy Exergy Economic GA optimization Dynamic analysis	–	19.2	310 / - / 110 / 2.5 / 1.5 /	✓/×/×/✓
M. Shoaei et al. [71]	2023	Geothermal Solar	Power	Geothermal Solar PV ORC Steam cycle Gas cycle	Energy Exergy Economic Environmental GA optimization	50.6	25.4	520 / - / - / - / - /	×/×/×/✓
R. Li et al. [72]	2023	Solar Geothermal	Power Freshwater	Solar tower Geothermal Dual loop OFC HDH MED	Energy Exergy Economic MOPSO optimization Dynamic analysis	–	22.4	750 / - / - / 100 / - /	✓/×/×/✓

findings are significant for advancing research in hybrid energy systems, contributing to a more sustainable and resilient energy future.

CRediT authorship contribution statement

Ali Shokri Kalan: Writing – original draft, Visualization, Validation, Supervision, Software, Methodology, Formal analysis, Data curation, Conceptualization. **Mohammadreza Babaei Khuyinrud:** Writing – original draft, Visualization, Validation, Software, Methodology, Formal analysis, Data curation, Conceptualization. **Farshad Jahangiri:** Writing – original draft, Validation, Software, Methodology, Formal analysis, Data curation. **Ramin Ahmadi:** Writing – original draft, Validation, Software, Methodology, Data curation. **Amir Mahboubi:** Writing – original draft, Validation, Software, Methodology. **Xiaoshu Lü:** Writing – review & editing, Visualization, Supervision, Conceptualization. **Marc A. Rosen:** Writing – review & editing, Supervision, Methodology, Conceptualization.

Declaration of competing interest

The authors declare that they have no known competing financial interests or personal relationships that could have appeared to influence the work reported in this paper.

Acknowledgement

The authors acknowledge the financial support provided by the **European Union's** Interreg Aurora (RESILIFY, Grant No. 20366468) and CETPartnership (OptiDCG4H2, Grant No. CETP-2023-00567, Enhance Europe CETP-2023-00061).

Appendix A. Supplementary data

Supplementary data to this article can be found online at https://doi.org/10.1016/j.apenergy.2025.126640.

Data availability

Data will be made available on request.

References

[1] Abrantes I, Ferreira AF, Magalhães LB, Costa M, Silva A. The impact of revolutionary aircraft designs on global aviation emissions. Renew Energy Mar. 2024;223:119937. https://doi.org/10.1016/J.RENENE.2024.119937.

[2] Rajabi MS, Moradi R. Fossil fuels reservoirs and extraction. Elsevier eBooks; Jun. 2023. p. 61–8. https://doi.org/10.1016/b978-0-323-93940-9.00044-x.

[3] Fu X, Zhang Y, Liu X, Liu Z. Stable power supply system consisting of solar, wind and liquid carbon dioxide energy storage. Renew Energy Feb. 2024;221:119730. https://doi.org/10.1016/J.RENENE.2023.119730.

[4] Rajabi M, Mehrpooya M, Haibo Z, Huang Z. Chemical looping technology in CHP (combined heat and power) and CCHP (combined cooling heating and power) systems: a critical review. Appl Energy Nov. 2019;253:113544. https://doi.org/10.1016/j.apenergy.2019.113544.

[5] Doninelli M, Morosini E, Gentile G, Putelli L, Di Marcoberardino Gioele, Binotti M, et al. Thermal desalination from rejected heat of power cycles working with CO_2-based working fluids in CSP application: a focus on the MED technology. Sustain Energy Technol Assess Dec. 2023;60:103481. https://doi.org/10.1016/j.seta.2023.103481.

[6] Oyekale J, Petrollese M, Cau G. Modified auxiliary exergy costing in advanced exergoeconomic analysis applied to a hybrid solar-biomass organic Rankine cycle plant. Appl Energy Jun. 2020;268:114888. https://doi.org/10.1016/j.apenergy.2020.114888.

[7] Mehrpooya M, Bahramian P, Pourfayaz F, Rosen MA. Introducing and analysis of a hybrid molten carbonate fuel cell-supercritical carbon dioxide Brayton cycle system. Sustain Energy Technol Assess Dec. 2016;18:100–6. https://doi.org/10.1016/j.seta.2016.10.003.

[8] Khuyinrud Mohammadreza Babaei, Kalan AS, Ghiasirad Hamed, Gholizadeh Towhid, Lü Xiaoshu, Arabkoohsar A. Exergoeconomic optimization and environmental analysis of a novel waste-to-energy cogeneration system with zeotropic mixtures as working fluids. Process Saf Environ Prot Mar. 2025:106976. https://doi.org/10.1016/j.psep.2025.106976.

[9] Mehrpooya M, Akbarpour S, Vatani A, Rosen MA. Modeling and optimum design of hybrid solid oxide fuel cell-gas turbine power plants. Int J Hydrog Energy 2014;39(36):21196–214. https://doi.org/10.1016/j.ijhydene.2014.10.077.

[10] Liu J, Hsu C-Y, Ahmad SF, Alotaibi MA, Allahham Mahmoud Izzat, Qin M. Design and energy, exergy, thermoeconomic, and exergo-environmental (4E) analyses of a novel hybrid geothermal/biogas-powered green multi-generation system using a post-combustion CO_2 capture unit. Appl Energy Oct. 2024;377:124662. https://doi.org/10.1016/j.apenergy.2024.124662.

[11] Tayerani Charmchi AS, Ifaei P, Yoo C. Smart supply-side management of optimal hydro reservoirs using the water/energy nexus concept: a hydropower pinch analysis. Appl Energy Jan. 2021;281:116136. https://doi.org/10.1016/j.apenergy.2020.116136.

[12] Mehrpooya M, Ghorbani B, Bahnamiri FK, Marefati M. Solar fuel production by developing an integrated biodiesel production process and solar thermal energy system. Appl Therm Eng Feb. 2020;167:114701. https://doi.org/10.1016/j.applthermaleng.2019.114701.

[13] Assareh Ehsanolah, Keykhah Abolfazl, Bedakhanian A, Agarwal N, Lee M. Optimizing solar photovoltaic farm-based cogeneration systems with artificial intelligence (AI) and cascade compressed air energy storage for stable power generation and peak shaving: a Japan-focused case study. Appl Energy Sep. 2024;377:124468. https://doi.org/10.1016/j.apenergy.2024.124468.

[14] Chen Y, Guo W, Lund PD, Du N, Yang K, wang J. Configuration optimization of a wind-solar based net-zero emission tri-generation energy system considering renewable power and carbon trading mechanisms. Renew Energy Oct. 2024;232:121086. https://doi.org/10.1016/J.RENENE.2024.121086.

[15] Wu J, Li R, Xiang Y, Wang S, Wang L, Li Q. Quantitative sustainability assessment and sensitivity analysis for a solar-driven combined heating and power system integrated with organic Rankine cycle and ground source heat pump. Appl Therm Eng Feb. 2023;220:119722. https://doi.org/10.1016/j.applthermaleng.2022.119722.

[16] Ghorbani S, Deymi-Dashtebayaz M, Dadpour D, Delpisheh M. Parametric study and optimization of a novel geothermal-driven combined cooling, heating, and power (CCHP) system. Energy Jan. 2023;263:126143. https://doi.org/10.1016/J.ENERGY.2022.126143.

[17] Qian J, Wu J, Yao L, Mahmut S, Zhang Q. Comprehensive performance evaluation of wind-solar-CCHP system based on emergy analysis and multi-objective decision method. Energy Sep. 2021;230:120779. https://doi.org/10.1016/J.ENERGY.2021.120779.

[18] Chen R, et al. Waste heat management of gas turbine-tailored power plants with reverse osmosis (RO) technology and hydrogen fuel production; sensitivity analysis and techno-economic optimization using genetic algorithm methods. Appl Therm Eng Jan. 2025;266:125590. https://doi.org/10.1016/J.APPLTHERMALENG.2025.125590.

[19] Forghani AH, Solghar AA, Hajabdollahi H. Optimal design of a multi-generation system based on solar and geothermal energy integrated with multi-effect distillatory. Appl Therm Eng Jan. 2024;236:121381. https://doi.org/10.1016/J.APPLTHERMALENG.2023.121381.

[20] Marefati M, Mehrpooya M. Introducing a hybrid photovoltaic solar, proton exchange membrane fuel cell and thermoelectric device system. Sustain Energy Technol Assess Dec. 2019;36:100550. https://doi.org/10.1016/j.seta.2019.100550.

[21] Ran P, Ou YF, Zhang CY, Chen YT. Energy, exergy, economic, and life cycle environmental analysis of a novel biogas-fueled solid oxide fuel cell hybrid power generation system assisted with solar thermal energy storage unit. Appl Energy Mar. 2024;358:122618. https://doi.org/10.1016/J.APENERGY.2024.122618.

[22] Mehrpooya M, Ghorbani B, Mousavi SA. Integrated power generation cycle (Kalina cycle) with auxiliary heater and PCM energy storage. Energy Convers Manag 2018;177:453–67. https://doi.org/10.1016/j.enconman.2018.10.002.

[23] Ma Y, Zhao M, Bai F, Yu R, Liu L, Wang J. Numerical simulation and experimental verification of solar PVT coupled PEM electrolyzer system for hydrogen production. Fuel Jun. 2024;365:131323. https://doi.org/10.1016/J.FUEL.2024.131323.

[24] Roy D, Samanta S. A solar-assisted power-to-hydrogen system based on proton-conducting solid oxide electrolyzer cells. Renew Energy Jan. 2024;220:119562. https://doi.org/10.1016/J.RENENE.2023.119562.

[25] Järvinen L, et al. Experimental study of alkaline water electrolyzer performance and frequency behavior under high frequency dynamic operation. Int J Hydrog Energy 2024;67:50–61. https://doi.org/10.1016/J.IJHYDENE.2024.04.093.

[26] Superchi F, Papi F, Mannelli A, Balduzzi F, Ferro FM, Bianchini A. Development of a reliable simulation framework for techno-economic analyses on green hydrogen production from wind farms using alkaline electrolyzers. Renew Energy May 2023;207:731–42. https://doi.org/10.1016/J.RENENE.2023.03.077.

[27] He Y, Guo S, Dong P, Wang C, Huang J, Zhou J. Techno-economic comparison of different hybrid energy storage systems for off-grid renewable energy applications based on a novel probabilistic reliability index. Appl Energy Dec. 2022;328:120225. https://doi.org/10.1016/J.APENERGY.2022.120225.

[28] Mirjalili S, Jangir P, Mirjalili SZ, Saremi S, Trivedi IN. Optimization of problems with multiple objectives using the multi-verse optimization algorithm. Knowl-Based Syst Oct. 2017;134:50–71. https://doi.org/10.1016/J.KNOSYS.2017.07.018.

[29] Águila-León J, Vargas-Salgado C, Díaz-Bello D, Montagud-Montalvá C. Optimizing photovoltaic systems: a meta-optimization approach with GWO-enhanced PSO algorithm for improving MPPT controllers. Renew Energy Sep. 2024;230:120892. https://doi.org/10.1016/J.RENENE.2024.120892.

[30] Mavromatidis G, Orehounig K, Carmeliet J. A review of uncertainty characterisation approaches for the optimal design of distributed energy systems. Renew Sust Energ Rev 2018;88:258–77. https://doi.org/10.1016/J.RSER.2018.02.021.

[31] Alonso-Travesset À, Coppitters D, Martín H, de la Hoz J. Economic and regulatory uncertainty in renewable energy system design: a review. Energies (Basel) 2023;16(2). https://doi.org/10.3390/en16020882.

[32] Hoang KT, Thilker CA, Knudsen BR, Imsland LS. A hierarchical framework for minimising emissions in hybrid gas-renewable energy systems under forecast uncertainty. Appl Energy Nov. 2024;373:123796. https://doi.org/10.1016/J.APENERGY.2024.123796.

[33] Padovan A, Del Col D, Sabatelli V, Marano D. DNI estimation procedures for the assessment of solar radiation availability in concentrating systems. Energy Procedia Jan. 2014;57:1140–9. https://doi.org/10.1016/J.EGYPRO.2014.10.100.

[34] Schwager C, Angele F, Nouri B, Schwarzbözl P, Teixeira Boura CJ, Herrmann U. Impact of DNI forecast quality on performance prediction for a commercial scale solar tower. SolarPACES Conf Proc 2024;1:1–9. https://doi.org/10.52825/solarpaces.v1i.675.

[35] Rostami S, Ghiasirad H, Rostamzadeh H, Kalan AS, Maleki A. A wind turbine driven hybrid HDH-MED-MVC desalination system towards minimal liquid discharge. S Afr J Chem Eng Apr. 2023;44:356–69. https://doi.org/10.1016/J.SAJCE.2023.03.007.

[36] Rostamzadeh H, Ghiasirad H, Amidpour M, Amidpour Y. Performance enhancement of a conventional multi-effect desalination (MED) system by heat pump cycles. Desalination Mar. 2020;477:114261. https://doi.org/10.1016/J.DESAL.2019.114261.

[37] Nondy J, Gogoi TK. Tri-objective optimization of two recuperative gas turbine-based CCHP systems and 4E analyses at optimal conditions. Appl Energy Oct. 2022;323:119582. https://doi.org/10.1016/J.APENERGY.2022.119582.

[38] Zare V, Hasanzadeh M. Energy and exergy analysis of a closed Brayton cycle-based combined cycle for solar power tower plants. Energy Convers Manag Nov. 2016;128:227–37. https://doi.org/10.1016/J.ENCONMAN.2016.09.080.

[39] Shokri Kalan A, Heidarabadi S, Khaleghi M, Ghiasirad H, Skorek-Osikowska A. Biomass-to-energy integrated trigeneration system using supercritical CO_2 and modified Kalina cycles: energy and exergy analysis. Energy May 2023;270:126845. https://doi.org/10.1016/J.ENERGY.2023.126845.

[40] Nondy J. 4E analyses of a micro-CCHP system with a polymer exchange membrane fuel cell and an absorption cooling system in summer and winter modes. Int J Hydrog Energy 2024;52:886–904. https://doi.org/10.1016/J.IJHYDENE.2023.06.220.

[41] Maryami R, Dehghan AA. An exergy based comparative study between LiBr/water absorption refrigeration systems from half effect to triple effect. Appl Therm Eng Sep. 2017;124:103–23. https://doi.org/10.1016/J.APPLTHERMALENG.2017.05.174.

[42] Rostamzadeh H, Rostami S. Performance enhancement of waste heat extraction from generator of a wind turbine for freshwater production via employing various nanofluids. Desalination Mar. 2020;478:114244. https://doi.org/10.1016/J.DESAL.2019.114244.

[43] Ghiasirad H, Rostamzadeh H, Nasri S. Design and evaluation of a new solar tower-based multi-generation system: Part II, exergy and Exergoeconomic modeling. In: Jabari F, Mohammadi-Ivatloo B, Mohammadpourfard M, editors. Integration of clean and sustainable energy resources and storage in multi-generation systems: Design, modeling and robust optimization. Cham: Springer International Publishing; 2020. p. 103–20. https://doi.org/10.1007/978-3-030-42420-6_6.

[44] Rostamzadeh H, Namin AS, Ghaebi H, Amidpour M. Performance assessment and optimization of a humidification dehumidification (HDH) system driven by absorption-compression heat pump cycle. Desalination Dec. 2018;447:84–101. https://doi.org/10.1016/J.DESAL.2018.08.015.

[45] Razmi A, Soltani M, Tayefeh M, Torabi M, Dusseault MB. Thermodynamic analysis of compressed air energy storage (CAES) hybridized with a multi-effect desalination (MED) system. Energy Convers Manag 2019;199:112047. https://doi.org/10.1016/J.ENCONMAN.2019.112047.

[46] Eisavi B, Ranjbar F, Nami H, Chitsaz A. Low-carbon biomass-fueled integrated system for power, methane and methanol production. Energy Convers Manag 2022;253:115163. https://doi.org/10.1016/J.ENCONMAN.2021.115163.

[47] Ren X, Li J, Pei G, Li P, Gong L. Parametric and economic analysis of high-temperature cascade organic Rankine cycle with a biphenyl and diphenyl oxide mixture. Energy Convers Manag 2023;276:116556. https://doi.org/10.1016/J.ENCONMAN.2022.116556.

[48] Colmenar-Santos A, Folch-Calvo M, Rosales-Asensio E, Borge-Diez D. The geothermal potential in Spain. Renew Sust Energ Rev Apr. 2016;56:865–86. https://doi.org/10.1016/J.RSER.2015.11.070.

[49] Aliahmadi M, Moosavi A, Sadrhosseini H. Multi-objective optimization of regenerative ORC system integrated with thermoelectric generators for low-temperature waste heat recovery. Energy Rep Nov. 2021;7:300–13. https://doi.org/10.1016/j.egyr.2020.12.035.

[50] Kalan AS, Ghiasirad H, Saray RK, Mirmasoumi S. Thermo-economic evaluation and multi-objective optimization of a waste heat driven combined cooling and power system based on a modified Kalina cycle. Energy Convers Manag 2021;247:114723. https://doi.org/10.1016/J.ENCONMAN.2021.114723.

[51] Bejan A, Tsatsaronis G, Moran MJ. Thermal design and optimization. In: Wiley-Interscience publication. Wiley; 1995 [Online]. Available: https://books.google.com/books?id=sTi2crXeZYgC.

[52] Palacios-Bereche R, Gonzales R, Nebra SA. Exergy calculation of lithium bromide–water solution and its application in the exergetic evaluation of absorption refrigeration systems LiBr-H_2O. Int J Energy Res 2012;36(2):166–81. https://doi.org/10.1002/er.1790.

[53] Turchi CS, Vidal J, Bauer M. Molten salt power towers operating at 600–650 °C: salt selection and cost benefits. Sol Energy Apr. 2018;164:38–46. https://doi.org/10.1016/j.solener.2018.01.063.

[54] Berkefeld Th, Schmidt D, Soltau D, von der Lühe O, Heidecke F. The GREGOR adaptive optics system. Astronomische Nachrichten 2012;333(9):863–71. https://doi.org/10.1002/asna.201211739.

[55] Jiménez-Torres M, Rus-Casas C, Lemus-Zúiga LG, Hontoria L. The importance of accurate solar data for designing solar photovoltaic systems—case studies in Spain. Sustainability 2017;9(2). https://doi.org/10.3390/su9020247.

[56] Jensen AR, et al. Pvlib iotools—open-source Python functions for seamless access to solar irradiance data. Sol Energy Dec. 2023;266:112092. https://doi.org/10.1016/J.SOLENER.2023.112092.

[57] Farr TG, Rosen PA, Caro E, Crippen R, Duren R, Hensley S, et al. The shuttle radar topography mission. Rev Geophys 2007;45(2). https://doi.org/10.1029/2005rg000183.

[58] CAMS radiation service - SoDa. SoDa. https://www.soda-pro.com/web-services/radiation/cams-radiation-service; 2025.

[59] Zhang T, Stackhouse PW, Macpherson B, Mikovitz J Colleen. A CERES-based dataset of hourly DNI, DHI and global tilted irradiance (GTI) on equatorward tilted surfaces: derivation and comparison with the ground-based BSRN data. Sol Energy May 2024;274:112538. https://doi.org/10.1016/J.SOLENER.2024.112538.

[60] Nourani V, Ahmadi R, Zhang Y, Dąbrowska D. Ensemble machine learning-based extrapolation of penman-Monteith-Leuning evapotranspiration data. Ecol Indic Jan. 2025;170:113012. https://doi.org/10.1016/J.ECOLIND.2024.113012.

[61] Hochreiter S, Schmidhuber J. Long short-term memory. Neural Comput Nov. 1997;9(8):1735–80. https://doi.org/10.1162/neco.1997.9.8.1735.

[62] Cho K, van Merrienboer Bart, Gulcehre C, Bahdanau D, Bougares F, Schwenk H, et al. Learning Phrase Representations using RNN Encoder–Decoder for Statistical Machine Translation. In: Proceedings of the 2014 Conference on Empirical Methods in Natural Language Processing (EMNLP); 2014. https://doi.org/10.3115/v1/d14-1179.

[63] Xiang Z, Yan J, Demir I. A rainfall-runoff model with LSTM-based sequence-to-sequence learning. Water Resour Res 2020;56(1):e2019WR025326. https://doi.org/10.1029/2019WR025326.

[64] Vahid Nourani A, Gholinia Peyman Abbaszadeh, Ahmadi R, Ke C-Q. Unravelling the impact of climate change and anthropogenic activities on streamflow: the benefit of newly developed evapotranspiration data. Hydrol Sci J Aug. 2024;69(14):2026–43. https://doi.org/10.1080/02626667.2024.2398654.

[65] Kratzert F, Klotz D, Brenner C, Schulz K, Herrnegger M. Rainfall–runoff modelling using long short-term memory (LSTM) networks. Hydrol Earth Syst Sci 2018;22(11):6005–22. https://doi.org/10.5194/hess-22-6005-2018.

[66] Zhang J, Zhu Y, Zhang X, Ye M, Yang J. Developing a long short-term memory (LSTM) based model for predicting water table depth in agricultural areas. J Hydrol (Amst) Jun. 2018;561:918–29. https://doi.org/10.1016/J.JHYDROL.2018.04.065.

[67] Mousavi Rabeti SA, Khoshgoftar Manesh MH, Blanco-Marigorta AM, Del Río-Gamero B. Multi-objective optimization, techno-economic analysis, and life cycle assessment of an innovative solar-biomass-driven cogeneration system integrated with MED-RO-MD: a case study of the Canary Islands. Renew Energy Jun. 2025:123757. https://doi.org/10.1016/j.renene.2025.123757.

[68] Yilmaz F, Jamil B. Parametric and a case study of an innovative solar-driven combined system: thermodynamic and environmental impact analysis for sustainable production of power, heating, and freshwater. Renew Energy Jan. 2025;238:121768. https://doi.org/10.1016/j.renene.2024.121768.

[69] Zhao L, Hai Q, Mei J. An integrated approach to green power, cooling, and freshwater production from geothermal and solar energy sources; case study of Jiangsu, China. Energy Jul. 2024:132304. https://doi.org/10.1016/j.energy.2024.132304.

[70] Cao Y, Dhahad HA, Sharma K, Anqi AE, El-Shafay AS, Najat Ahmed Ahmed. Comprehensive thermodynamic and economic analyses and optimization of a novel poly-generation setup utilizing solar and geothermal sources. Appl Therm Eng 2022;207:118133. https://doi.org/10.1016/j.applthermaleng.2022.118133.

[71] Shoaei M, Hajinezhad A, Moosavian SF. Design, energy, exergy, economy, and environment (4E) analysis, and multi-objective optimization of a novel integrated energy system based on solar and geothermal resources. Energy Oct. 2023;280:128162. https://doi.org/10.1016/j.energy.2023.128162.

[72] Li R, Xu D, Tian H, Zhu Y. Multi-objective study and optimization of a solar-boosted geothermal flash cycle integrated into an innovative combined power and desalinated water production process: application of a case study. Energy Nov. 2023;282:128706. https://doi.org/10.1016/j.energy.2023.128706.